

A cellular hierarchy in melanoma uncouples growth and metastasis

<https://doi.org/10.1038/s41586-022-05242-7>

Received: 1 July 2020

Accepted: 17 August 2022

Published online: 21 September 2022

 Check for updates

Panagiotis Karras^{1,2}, Ignacio Bordeu^{3,4,22,26}, Joanna Pozniak^{1,2,26}, Ada Nowosad^{1,2,26}, Cecilia Pazzi^{1,2}, Nina Van Raemdonck^{1,2}, Ewout Landeloos^{1,2}, Yannick Van Herck⁵, Dennis Pedri^{1,2}, Greet Bervoets^{1,2}, Samira Makhzami^{1,2}, Jia Hui Khoo⁶, Benjamin Pavie^{7,8,9}, Jochen Lamote¹⁰, Oskar Marin-Bejar^{1,2}, Michael Dewaele^{1,2}, Han Liang⁶, Xingju Zhang⁶, Yichao Hua^{2,11}, Jasper Wouters^{12,13}, Robin Browaeys^{14,15}, Gabriele Bergers^{2,11}, Yvan Saeys^{14,15}, Francesca Bosisio¹⁶, Joost van den Oord¹⁶, Diether Lambrechts^{17,18}, Anil K. Rustgi¹⁹, Oliver Bechter⁵, Cedric Blanpain²⁰, Benjamin D. Simons^{3,4,21}, Florian Rambow^{1,2,23,24,25} & Jean-Christophe Marine^{1,2}✉

Although melanoma is notorious for its high degree of heterogeneity and plasticity^{1,2}, the origin and magnitude of cell-state diversity remains poorly understood. Equally, it is unclear whether growth and metastatic dissemination are supported by overlapping or distinct melanoma subpopulations. Here, by combining mouse genetics, single-cell and spatial transcriptomics, lineage tracing and quantitative modelling, we provide evidence of a hierarchical model of tumour growth that mirrors the cellular and molecular logic underlying the cell-fate specification and differentiation of the embryonic neural crest. We show that tumorigenic competence is associated with a spatially localized perivascular niche, a phenotype acquired through an intercellular communication pathway established by endothelial cells. Consistent with a model in which only a fraction of cells are fated to fuel growth, temporal single-cell tracing of a population of melanoma cells with a mesenchymal-like state revealed that these cells do not contribute to primary tumour growth but, instead, constitute a pool of metastatic initiating cells that switch cell identity while disseminating to secondary organs. Our data provide a spatially and temporally resolved map of the diversity and trajectories of melanoma cell states and suggest that the ability to support growth and metastasis are limited to distinct pools of cells. The observation that these phenotypic competencies can be dynamically acquired after exposure to specific niche signals warrant the development of therapeutic strategies that interfere with the cancer cell reprogramming activity of such microenvironmental cues.

Considerable evidence indicates that melanoma cells can exhibit either a proliferative (or melanocytic) or a mesenchymal-like (or invasive) transcriptional cell state^{1,2}. Single-cell RNA-sequencing (scRNA-seq) analyses confirmed the coexistence of these two cell states in clinical samples^{3–5}. However, recent data from in vitro and in vivo models suggested that additional melanoma cell states may exist^{1,4,6}, and that our current view of melanoma intratumour heterogeneity is probably incomplete. These observations also raised the possibility that these distinct cell states may not contribute equally to tumour growth and metastatic spreading. An in-depth dissection of melanoma phenotypic heterogeneity in the in vivo relevant context is therefore needed.

Revisiting melanoma cell-state diversity

Although mouse models have been instrumental in understanding melanoma biology⁷, their ability to recapitulate the phenotypic

diversity observed in human patients remains unclear. We tested this in a spontaneous mouse model carrying the *Tyr::NRAS*^{Q61K/c} allele⁸ and lacking *Cdkn2a* (also known as *Ink4a* or *p16*^{INK4a})⁹. These mice develop cutaneous monoclonal melanoma lesions and, subsequently, lymph node, liver and lung metastases. To increase the versatility of this model, we derived syngeneic lines in C57BL/6 mice, and assessed the transcriptomic landscape of such melanoma lesions using scRNA-seq. Using published cell-type-specific gene sets, we identified T cell, B cell, cancer-associated fibroblast, dendritic cell, monocyte/macrophage, endothelial cell (EC), pericyte and malignant populations^{10–13} (Extended Data Fig. 1a), therefore highlighting the presence of a complex tumour microenvironment. To refine malignant cell typing, we selected cells expressing a melanoma-specific gene signature and exhibiting high copy-number variation, which was inferred using HoneyBadger¹⁴ (Extended Data Fig. 1b,c). About 35% of cells were annotated as malignant. Unsupervised Louvain-based clustering and uniform manifold

A list of affiliations appears at the end of the paper.

approximation and projection (UMAP) identified seven distinct melanoma cell states that were all detected in each lesion ($n = 5$) analysed (Fig. 1a and Extended Data Fig. 1d).

MITF is a key regulator of the differentiation status of melanoma^{1,15,16}. It induces genes implicated in melanogenesis, the primary differentiation-associated function of melanocytes, and low MITF leads to dedifferentiation. A wide range of *Mitf* levels and transcriptional activities were detected across all malignant cells (Fig. 1b). Distinct transcriptional programs have been associated with differential levels of MITF activity, namely the melanocytic/proliferative (MITF high, PRO) and mesenchymal-like/invasive (MITF low; INV) signatures. Melanoma cells expressing these signatures were readily detectable in the *NRAS*^{Q61K}/*Ink4a*^{-/-} lesions (Extended Data Fig. 1e). Notably, cells from cluster 4 exhibited the lowest MITF activity, indicating that these cells are the most dedifferentiated of all malignant cells (Fig. 1b).

Differential gene expression analysis resulted in characteristic gene lists, and SCENIC¹⁷ identified specific regulons for each cell state (Extended Data Fig. 1f and Supplementary Table 1). Gene set enrichment tools were used to functionally annotate each cluster (Fig. 1c and Supplementary Table 2). A gene expression signature for each of these clusters was then established (Fig. 1d and Supplementary Table 3), its activity was measured using AUCell¹⁷ and it was projected onto UMAP space (Fig. 1e). This analysis highlighted a transcriptional heterogeneity that goes beyond the melanocytic (cluster 0) and mesenchymal-like (cluster 6) subpopulations. Cells from clusters 4 and 1 shared markers of dedifferentiated neural crest (NC) stem-like cells (NCSCs), such as *Gfra2*, *Aqp1* or *Mef2c* (Extended Data Fig. 1g). Although largely overlapping, these two NC-like cell populations presented distinct features. Cells from cluster 4, in addition to expressing pluripotency markers such as *Sox2* or *Klf4* (Supplementary Table 1), uniquely expressed a distinct set of markers, including *Notch3*, *Nestin* (also known as *Nes*) or *Vcan* (Extended Data Fig. 1g). Notably, the transcriptome of these cells was reminiscent of that found in a pre-epithelial–mesenchymal transition (pre-EMT) (pre-migratory) NC stem cell population described recently¹⁸. These pre-migratory cells are the first NC-committed cells to emerge embryonically and constitute a pool of self-renewing NC stem cells¹⁹ (Fig. 1f). The second population to emerge during development—the delaminating NC population—mapped to cells from clusters 0 and 6, corresponding to the NCSC state described previously^{4,20}. As NC progenitors migrate, they acquire features of more mature derivatives, with one population moving towards a mesenchymal fate. These cells activate a transcriptional program that was similar to the melanoma mesenchymal-like cell signature (cluster 6). Thus, melanoma cells can hijack the molecular logic underlying the NC cell-fate specification program and dedifferentiate all the way back to a pre-EMT NC stem-like state. By doing so, these cells may acquire stem-cell-like phenotypic properties.

Given the high prevalence of *BRAF* mutations in human melanoma, we also profiled lesions arising in the commonly used *Tyr::cre*^{ERT2}/*Braf*^{V600E/+}/*Pten*^{fl} mouse model²¹. scRNA-seq revealed that these lesions comprise cells with contrasting *Mitf* levels (Extended Data Fig. 2a). Importantly, melanoma cells exhibiting the melanocytic, mesenchymal-like, NC-like and pre-EMT NC stem-like signatures could also be identified in these lesions (Fig. 1g). We measured the mouse *NRAS* malignant cell-state signatures in a large scRNA-seq dataset from treatment-naive human metastatic melanoma biopsies²² (Extended Data Fig. 2b). As expected, the melanocytic and mesenchymal-like cell states were identified in multiple patients. We also examined a previously reported scRNA-seq dataset^{10,11} containing few primary lesions (Extended Data Fig. 2c). Most malignant transcriptional cell states, defined by the clustering analysis of the mouse lesions, were identified in both primary and metastatic human melanoma lesions from both cohorts and, therefore, irrespective of their oncogenic driver mutations (Fig. 1g and Extended Data Fig. 2c).

A cellular hierarchy in melanoma

Given their transcriptomic diversity, we questioned whether the growth of these primary melanomas might be hierarchically organized. We turned to an inducible genetic lineage-tracing approach based on the multicolour *Rosa26-LSL-Confetti*²³ allele, which enables the stochastic expression of up to ten different colour combinations, and the tamoxifen (TAM)-inducible *cre*^{ERT2} allele under the control of the melanocytic promoter *Tyr::cre*^{ERT2} (ref. 7). The *Tyr::NRAS*^{Q61K}/*Ink4a*^{-/-}/*Tyr::cre*^{ERT2/+}/*Rosa26*^{LSL-Confetti/+} compound mice (Fig. 2a) developed primary melanoma lesions at around 8 ± 2 months of age. Tumour pieces of primary lesions were transplanted into cohorts of C57BL/6 mice and lesions grew steadily with a slow, exponential-like, growth characteristic with tumour-to-tumour variability in the expansion rate (Fig. 2b). These lesions were histologically indistinguishable from their tumour of origin and expressed heterogeneous melanocytic patterns (Extended Data Fig. 3a,b). Titrating down the dose of TAM, we were able to reach clonal density (Extended Data Fig. 3c) while maintaining the expected colour mosaicism²⁴ (Extended Data Fig. 3d,e).

To gain insights into the overall growth pattern, we examined the distribution of marked cells from 2D sections. We found that a small fraction of clones grew large, spanning tens of cells or more, whereas the majority of clones remained very small, containing few cells (Fig. 2c and Extended Data Fig. 3f).

We next used a more rigorous density-based method of assignment to serially reconstruct and score total clone sizes at the single-cell resolution using 3D confocal imaging (Fig. 2d and Extended Data Fig. 4a). Once again, we found significant heterogeneity in clone size across all of the tumour samples (Fig. 2e and Supplementary Table 4). Further evidence of bimodal behaviour was visible in the cumulative distribution of clone sizes (Fig. 2f, Extended Data Fig. 4b–e, Supplementary Table 5 and Supplementary Note). Such behaviour was consistent with a proliferative hierarchy in which a stem-cell-like population, S, expands stochastically through cell duplication, while giving rise to a second progenitor cell-like state, P, which in turn expands through cell duplication (Fig. 2g and Supplementary Note).

Statistical analysis confirmed that the minimal hierarchical model could capture quantitatively the wide range of clone size data across all of the tumour samples with stem and progenitor cell expansion rates that were sample specific but broadly $\Delta_S \approx 0.09$ and $\Delta_P \approx 0.04$ per day, respectively (Fig. 2g, Extended Data Fig. 4f–k, Supplementary Table 5 and Supplementary Note). Moreover, the analysis indicated that, after a tenfold expansion in tumour size, around 10–32% of the surviving clones were stem-cell-derived with the remainder arising from progenitors (or non-cycling cells). Considering possible P-cell-derived clone loss, such a figure was broadly consistent with the estimated abundance ($6 \pm 3\%$) of pre-EMT NC stem-like population based on scRNA-seq data, raising the possibility that this population may function as melanoma stem cells.

We also examined the proliferation kinetics of tumour growth using consecutive pulses of cell labelling with 5-ethynyl-2'-deoxyuridine (EdU) and bromodeoxyuridine (BrdU) (Fig. 2h). The EdU⁺ and BrdU⁺ cell fractions scaled in approximate proportion to the incorporation time, consistent with the majority of the tumour being comprised of proliferative cells dividing at a similar rate. Moreover, with the fraction of double-positive cells being approximately equal to the product of the individual fractions, these results supported the prediction of the model that tumour growth is maintained by cells dividing stochastically at a similar slow average rate (Fig. 2i). Finally, with S phase estimated at around 6–8 hours, these results pointed to an average cell division rate of approximately once per 30 days, a figure broadly consistent with the tracing analysis.

We performed similar lineage-tracing experiments after transplantation of tumours into immunocompromised mice (Extended

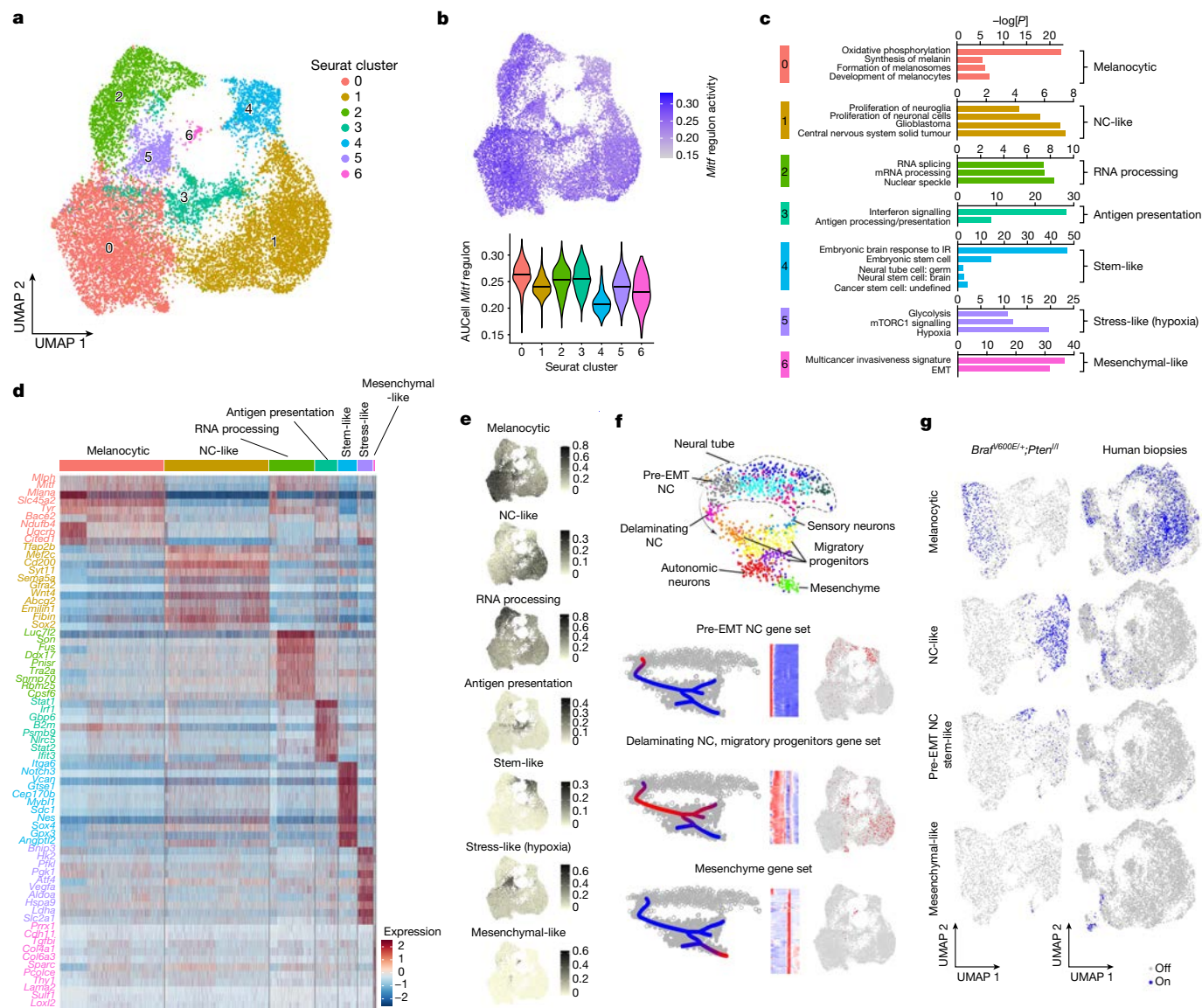


Fig. 1 | Single-cell transcriptomic landscape of *NRAS*-driven melanoma.
a, UMAP analysis of malignant cells analysed by scRNA-seq and integrated across five different *NRAS*^{Q61K/+}; *Ink4a*^{-/-} primary lesions. **b**, *Mitf* regulon activity in mouse malignant cells projected as UMAP (top) and a violin plot (bottom). The centre lines in the violin plots represent the median. **c**, Functional enrichment terms of the characteristic Seurat clusters identified in **a**. *P* values were determined using two-tailed Fisher's exact tests. **d**, Discriminative marker genes (*n* = 9) for each functionally enriched state. **e**, The AUCell scores (colour

scale) of the top functionally enriched marker genes per state projected on malignant UMAP (Supplementary Table 1). **f**, Mapping of gene expression program activities during mouse NC development¹⁸ onto transcriptional states of *NRAS*^{Q61K/+}; *Ink4a*^{-/-} melanoma. **g**, The activity (binary AUCell score) of selected mouse malignant gene signatures from *NRAS*^{Q61K/+}; *Ink4a*^{-/-} melanoma projected onto scRNA-seq datasets from *Braf*^{V600E/+}; *Pten*^{+/l} mouse melanoma lesions (left) and human clinical metastatic melanoma samples²² (right).

Data Fig. 5a–e). Qualitative analysis of the 2D cluster size distribution was similar compared to that observed in the immune-proficient background (Extended Data Fig. 5f). Notably, however, tumours grew more rapidly on this background (Extended Data Fig. 5b), indicating that the adaptive immune system does not affect the mode of tumour growth per se but, instead, restrains the overall growth by keeping in check the effective proliferation rate of each malignant compartment.

These results support a model in which primary melanoma is organized in a cellular hierarchy, comprising at least two distinct populations—a stem-cell-like and progenitor-cell-like population—that exhibit different growth kinetics and fate behaviour. On the basis of the scRNA-seq analysis, we hypothesized that the S population might overlap with the pre-EMT NC stem-like population. The spatial organization

and dispersion of clones was suggestive of a niche-like organization in which stem cell competence is associated with a spatially localized environment.

ECs promote melanoma growth

To search for evidence of a niche-like organization that could support a pre-EMT NC stem-like population, we used spatially resolved unsupervised transcriptomics (Fig. 3a). The spatial transcriptomics data were integrated with the scRNA-seq data using Seurat (v.3) anchor-based integration²⁵. A pathologist (J.v.d.O.) annotated various histopathological features on each section. This analysis revealed an expected positive correlation between the stress-like (hypoxia) prediction score and the distance to the nearest blood

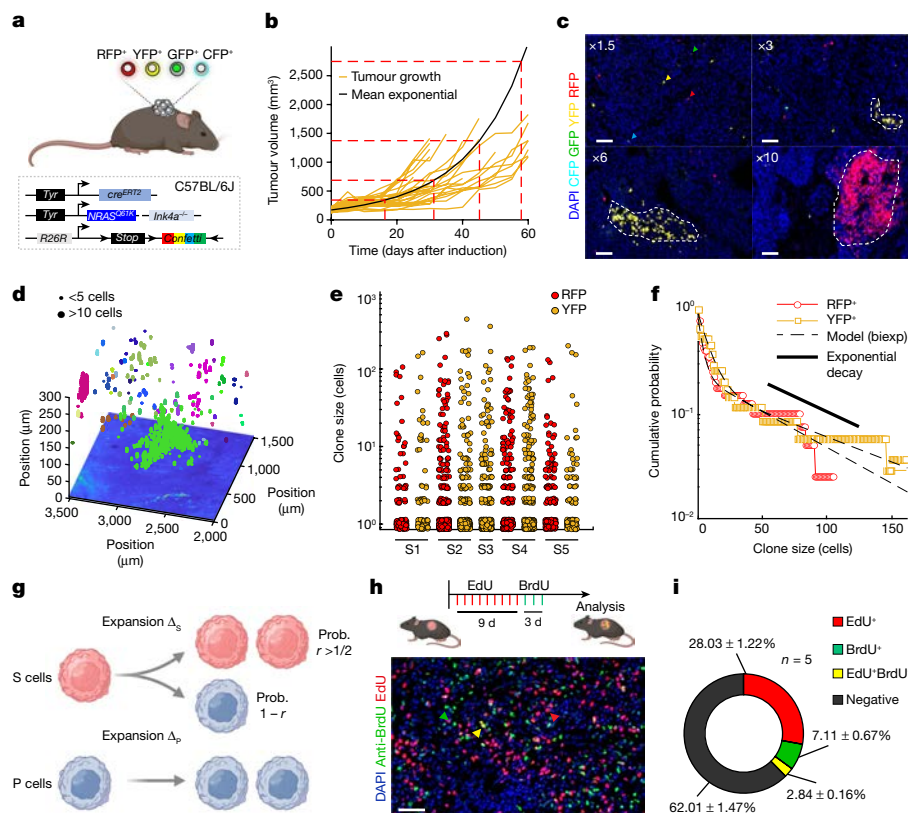


Fig. 2 | Multicolour lineage tracing reveals that melanoma growth is hierarchically organized. **a**, Schematic of the mouse model. **b**, Tumour growth kinetics (mm^3) of individual tumours (yellow), and the corrected mean obtained from extrapolating the missing time points using the model prediction (black curve). **c**, Confocal images of melanomas exhibiting Confetti expression at different relative growths after TAM administration (0.5 mg). Representative images from at least 8 mice per group. Scale bars, 100 μm . **d**, Representative reconstruction of 3D clones. Independent clones appear in different colours. A single z-slice of the corresponding dataset is shown at the bottom of the plot. **e**, The distribution of clone sizes by sample and by channel obtained from five cleared tumours (Supplementary Table 5). **f**, Cumulative distribution, showing the probability (prob.) of observing a clone larger than a given size. The corresponding biexponential (biexp) fits (dashed line; $R^2 = 0.96$;

s.e. of the fit $S = 0.03$) and exponential decay of the tail (black line) are shown. **g**, Schematics of the minimal hierarchical model. The parameters Δ_s and Δ_p correspond to the expansion rates of the S and P populations, respectively. Although the data could accommodate a line of fit parameters, fixing the relative transition rate of stem cells into the progenitor cell compartment, $r = 0.75$, the model shows an excellent fit to the data with $\Delta_s \approx 0.09$ and $\Delta_p \approx 0.04$ and a stem fraction $f_s \approx 0.21$ or 21% (see Supplementary Note). **h**, The experimental procedure for the dual pulse labelling assay using EdU and BrdU (top). Bottom, image of double BrdU (green) and EdU (red) immunostaining. Representative image from $n = 5$ tumours. Scale bar, 50 μm . **i**, The percentage of single- and double-labelled cells. Quantification was assessed from five different mice and four technical replicates per mouse. The schematics in **a**, **g** and **h** were generated using BioRender.

vessels (Extended Data Fig. 6a,b). By contrast, an inverse correlation was found between the distance to the nearest blood vessel and the pre-EMT NC stem-like prediction score (Fig. 3b and Extended Data Fig. 6c).

To substantiate this finding, we applied spatially enhanced resolution omics-sequencing (stereo-seq), a method that enables transcriptomic profiling with high resolution and sensitivity²⁶. We segmented the data into 50×50 DNA nanoball bins to retrieve transcriptomic information for 51,200 bins of 25 μm diameter (Extended Data Fig. 6d–f). Measuring a transcriptional endothelial signature (binary AUCell cut-off) revealed the location of the tumour vasculature (Fig. 3c and Supplementary Table 6), of which the external boundaries largely mirrored those that were manually annotated by our pathologist. We assigned cell identities to each spatial module and, therefore, confirmed the significant negative correlation between the pre-EMT NC stem-like state and distance to the nearest blood vessel (Fig. 3d), as well as the positive correlation between the stress-like (hypoxia) cell state and blood vessels (Extended Data Fig. 6g).

To validate these locations at a true single-cell resolution, we used Molecular Cartography. In each section, we examined the expression of genes chosen to distinguish cellular compartments of the tumour

microenvironment and various melanoma cell states (Supplementary Table 7). A computational framework that automatically computes cell segmentation and annotation was developed (Extended Data Fig. 6h). Approximately 109,000 malignant cells were identified, among which about 900 cells expressed multiple pre-EMT NC stem-like markers, including *Notch3*, *Nes*, *Vcan*, *Dusp15* and *Celf5* (cluster 23; Extended Data Fig. 6i–k). A total of 90% of cells from cluster 23 co-expressed *Sox10* and all three pre-EMT NC stem-like markers *Notch3*, *Vcan* and *Nes*. A similar approach was used to annotate the stress-like (hypoxia) cell population (cluster 1; Extended Data Fig. 6l). Both melanoma cell populations were then pseudocoloured (Fig. 3e), and their distance to the nearest blood vessel was quantified (Fig. 3f). The median distance to the nearest blood vessel for pre-EMT NC stem-like cells was significantly shorter than that for those annotated as stress-like (hypoxia). Note that similar conclusions could be drawn when analysing the localization of cells positive for *Sox10* and only one of the pre-EMT NC stem-like markers, such as *Notch3*, *Nes* or *Vcan*, for example (Extended Data Fig. 6m). An enrichment of cells positive for both *Sox10* and *Notch3* in blood-vessel-containing areas was further confirmed by RNAscope (Extended Data Fig. 6n,o) and by immunohistochemistry (Fig. 3g) analysis.

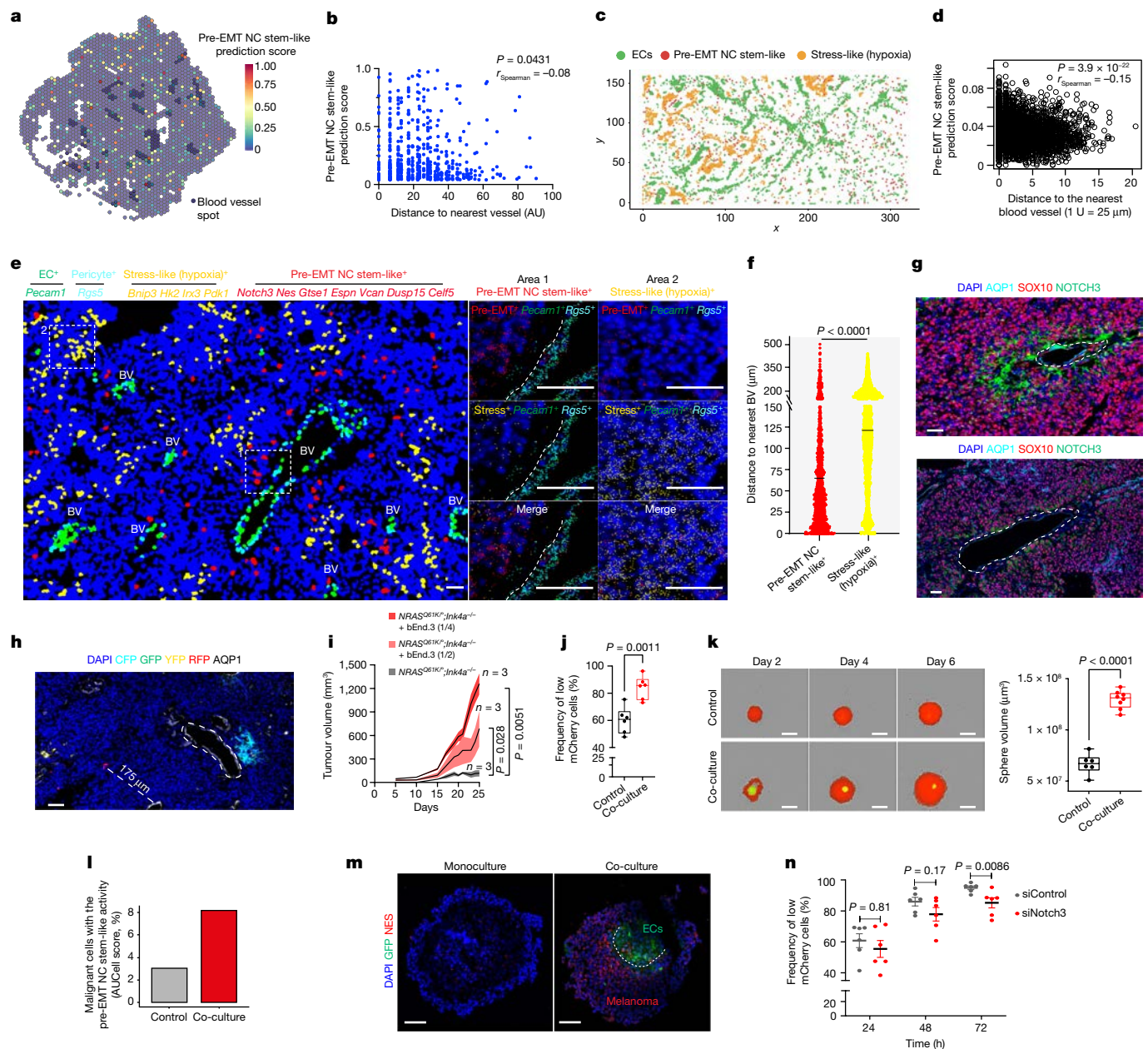


Fig. 3 | A perivascular niche promotes melanoma growth. a, Quantification of pre-EMT NC stem-like activity onto spatial transcriptomics. Dark blue, blood vessel annotation. **b**, Inverse correlation (Spearman) between the pre-EMT NC stem-like prediction score and the distance to the nearest blood vessel. AU, arbitrary units. **c**, Spatial scatter plot showing bins of EC, pre-EMT NC stem-like and hypoxia (binary AUCell score) populations. **d**, Anti-correlation (Spearman) of pre-EMT NC stem-like activity (AUCell score) and the distance to the closest blood vessel. **e**, Molecular cartography for the indicated genes. Left, pseudocoloured cells based on the type/state identity ($n = 33$ regions of interest (ROIs)). Insets: areas enriched for either pre-EMT NC stem-like (area 1) or stress-like (hypoxia, area 2) cells. Scale bars, 50 μm . **f**, The median distance to the nearest blood vessel ($n = 33$ ROIs; $P < 0.0001$). **g**, Immunostaining for the indicated proteins. Top, a capillary. Bottom, a dilated tumour blood vessel ($n = 3$ tumours). Scale bars, 50 μm . **h**, Confocal image of Confetti⁺ tumours ($n = 6$) that were immunostained for AQP1. Scale bar, 50 μm . **i**, DsRed-labelled melanoma cells were injected into immunocompromised mice alone or with GFP-labelled bEnd.3 ECs (ratio 1/2, $P = 0.0281$; and ratio 1/4, $P = 0.0051$). **j**, Tumour volume as a function of time (days) ($n = 3$). Data are mean \pm s.e.m. **k**, The percentage of mCherry high versus low watermelon⁺ cells cultured alone or with bEnd.3 cells ($n = 6$, $P = 0.0011$). **l**, Melanospheres (DsRed-labelled) grown alone or with (GFP-labelled) bEnd.3 ECs (left). Right, melanosphere volume ($n = 6$ monocultures, $n = 8$ co-cultures; $P < 0.0001$). Scale bars, 300 μm . **m**, Melanoma cells were cultured alone (control) or with bEnd.3 cells, and the percentage of malignant cells with the pre-EMT NC stem-like state (binary AUCell score) was determined using scRNA-seq. **n**, Representative images of melanospheres ($n = 2$) grown alone or with GFP-labelled bEnd.3 cells. The presence of NES⁺ cells was evaluated. Scale bars, 50 μm . **o**, Doxycycline-induced watermelon⁺ cells were transfected with siControl or siNotch3 supplemented with bEnd.3 cells. P values were determined using two-tailed Fisher's exact tests (**b** and **d**), two-tailed Mann-Whitney U -tests (**f**, **i** and **n**) and unpaired two-tailed Student's t -tests with Welch's correction (**j** and **k**). In **j** and **k**, the boxes extend from the 25th to 75th percentile, the centre lines represent the median, and the whiskers represent minimum to maximum values.

Tumour volume as a function of time (days) ($n = 3$). Data are mean \pm s.e.m. **j**, The percentage of mCherry high versus low watermelon⁺ cells cultured alone or with bEnd.3 cells ($n = 6$, $P = 0.0011$). **k**, Melanospheres (DsRed-labelled) grown alone or with (GFP-labelled) bEnd.3 ECs (left). Right, melanosphere volume ($n = 6$ monocultures, $n = 8$ co-cultures; $P < 0.0001$). Scale bars, 300 μm . **l**, Melanoma cells were cultured alone (control) or with bEnd.3 cells, and the percentage of malignant cells with the pre-EMT NC stem-like state (binary AUCell score) was determined using scRNA-seq. **m**, Representative images of melanospheres ($n = 2$) grown alone or with GFP-labelled bEnd.3 cells. The presence of NES⁺ cells was evaluated. Scale bars, 50 μm . **n**, Doxycycline-induced watermelon⁺ cells were transfected with siControl or siNotch3 supplemented with bEnd.3 cells. P values were determined using two-tailed Fisher's exact tests (**b** and **d**), two-tailed Mann-Whitney U -tests (**f**, **i** and **n**) and unpaired two-tailed Student's t -tests with Welch's correction (**j** and **k**). In **j** and **k**, the boxes extend from the 25th to 75th percentile, the centre lines represent the median, and the whiskers represent minimum to maximum values.

We next performed immunohistochemistry analysis using thick (>2 mm Breslow) primary nodular human melanoma biopsies ($n = 13$). Cells positive for both SOX10 and VCAN could be identified in 12 out of

13 lesions and their proportion ranged from rare (less than 1%, in 7 out of 13 lesions) to more frequent (between 1 and 5%, in 5 out of 13 lesions). Importantly, these cells occurred in clusters and a fraction localized in

proximity to CD31⁺ blood vessels (Extended Data Fig. 7a). Additional staining confirmed the presence of SOX10⁺NES⁺ double-positive cells in the vicinity of the tumour vasculature (AQPI⁺, 7 out of 8 lesions) and therefore irrespective of the *NRAS* or *BRAF* status (Extended Data Fig. 7a).

These findings support a model in which pre-EMT NC stem-like tumour cells localize preferentially at perivascular regions where they renew, producing more S cells that expand to colonize further the vasculature, or detach, giving rise to P-type cells that move away from the niche (Extended Data Fig. 7b). Consistently, we found that the productive Confetti-positive clones were typically either in contact with or in close vicinity to the tumour vasculature (Fig. 3h and Extended Data Fig. 7c, d).

ECs were shown to promote the propagation of brain tumours²⁷. To test whether ECs also support the *in vivo* growth of melanoma, we co-injected DsRed⁺ *NRAS*^{Q61K}/*Ink4a*^{-/-} mouse melanoma cells either alone or with GFP⁺ ECs (bEnd.3) in immunocompromised mice (Extended Data Fig. 8a). Co-injection of ECs enhanced xenograft growth in a cell-dose-dependent manner (Fig. 3i) and, ultimately, decreased the overall survival (Extended Data Fig. 8b). bEnd.3 ECs also stimulated the 2D and 3D (melanospheres) *in vitro* growth of melanoma cells (Fig. 3j,k, Extended Data Fig. 8c,d, Methods and Supplementary Fig. 1).

After the co-culturing of melanoma and bEnd.3 cells, we analysed the cellular composition using scRNA-seq (Extended Data Fig. 8e). Although the parental *NRAS*^{Q61K}/*Ink4a*^{-/-} cell line contained more than 90% of cells in the melanocytic cell state, the presence of bEnd.3 cells caused the emergence of cells with the dedifferentiated NC-like and pre-EMT NC stem-like signatures (Fig. 3l and Extended Data Fig. 8f,g). Moreover, Nes⁺ cells emerged in melanospheres grown in the presence of bEnd.3/GFP ECs (Fig. 3m and Extended Data Fig. 8h). These data indicated that ECs contribute to a niche environment that promotes dedifferentiation of melanoma cells and, thereby, stimulate melanoma growth.

To dissect the molecular mechanisms underlying the growth-promoting activity of ECs, we used NicheNet²⁸ and CellChat²⁹, two different computational approaches that predict cell-to-cell communications. We identified cell-type-enriched ligands and searched for matching receptors that are expressed selectively in the pre-EMT NC stem-like cells. A putative interaction was identified between the *Dll4*-expressing ECs and the NOTCH3 receptor was specifically expressed in pre-EMT NC stem-like cells (Extended Data Fig. 8i-l). Notably, significant overlaps were detected when comparing genes upregulated in the pre-EMT NC stem-like melanoma cells with those from the reactome-based NOTCH signalling signature (Gene Set Enrichment Analysis Molecular Signature Database (GSEA-MSIGDB): M10189)³⁰ and genes induced in synovial fibroblasts after DLL4 stimulation³¹ (Extended Data Fig. 8m), indicating that the DLL4–NOTCH3 interaction leads to the activation of NOTCH signalling. Consistently, expression of the co-factor *Rbpj* of the active intracellular domain of NOTCH was enriched in the pre-EMT NC stem-like cells (Extended Data Fig. 8n). To test whether the growth-stimulating activity of ECs was dependent on the activation of NOTCH signalling, we silenced *Notch3* in melanoma cells. Notably, the growth of *Notch3* knockdown melanoma cells was no longer stimulated by the presence of bEnd.3 ECs (Fig. 3n). Together these data support a model in which ECs stimulate melanoma growth by promoting emergence and/or maintenance of the pre-EMT NC stem-like state.

PRRX1 marks cells that fuel metastasis

Unsupervised analysis predicted that PRRX1, which is known to promote epithelial-to-mesenchymal transition (EMT) in epithelial cancers^{32,33}, is a putative driver of both mouse and human mesenchymal-like cells (Fig. 4a and Extended Data Fig. 9a,b). *PRRX1* was also highly expressed and/or transcriptionally active in freshly

isolated clinical biopsies, The Cancer Genome Atlas skin cutaneous melanoma human clinical samples, melanoma cell lines and short-term cultures (MM lines) with the invasive/undifferentiated melanoma signature^{34–36} (Extended Data Fig. 9c–e). A set of common mouse and human PRRX1-target genes was identified, which includes *FBN1* and *TGFB1* (Fig. 4a). Consistently, *PRRX1* expression and activity was progressively increased in melanocytic melanoma lines (MM057, MM074, MM087) after *SOX10* knockdown, which leads to a progressive reprogramming into mesenchymal-like cells⁶ (Extended Data Fig. 9f). Moreover, silencing *PRRX1* in mesenchymal-like melanoma cultures caused a substantial decrease in the mesenchymal and EMT signatures (Fig. 4b) that was accompanied by a decreased ability to invade in short-term *in vitro* migration assays (Extended Data Fig. 9g,h). These data indicate that PRRX1 may not only mark the melanoma mesenchymal-like cell population, but also contribute to the acquisition and/or maintenance of the mesenchymal-like phenotype.

Taking advantage of the *Prrx1-cre^{ER}-Ires-GFP³⁷* mice, we next devised a strategy to fate map *Prrx1*-positive cells *in vivo*. We generated *Tyr::NRAS^{Q61K}; Ink4a^{-/-}; Prrx1-cre^{ER}-Ires-GFP; Rosa26^{-LSL-tdTomato}* (hereafter Met-Track) mice (Fig. 4c). As expected, these mice developed primary melanomas, and a small fraction of GFP⁺ cells could be detected in the deeper part (for example, the dermis or subcutaneous tissues) of these lesions (data not shown). Several rounds of TAM administrations ensured that the GFP⁺ cells turned on tdTomato expression (Fig. 4c,d). Although all *Prrx1* progenies are expected to remain tdTomato positive, a fraction of these cells may lose GFP expression owing to their transcriptional reprogramming into *Prrx1*-negative cells. We sorted tdTomato⁺ cells using fluorescence-activated cell sorting (FACS) shortly after TAM exposure and analysed the cell composition using scRNA-seq (Methods and Supplementary Fig. 2). All of the malignant tdTomato⁺ cells, which maintained low levels of expression of lineage marker genes (Extended Data Fig. 10a), expressed high levels of *Prrx1* and other mesenchymal-like markers (Extended Data Fig. 10b). Consistently, high *Prrx1* regulon activity, as well as elevated expression levels of an EMT gene signature (GSEA-MSIGDB: M5930), were detected in these cells (Fig. 4e). Critically, none of these cells co-expressed pre-EMT NC stem-like markers (Extended Data Fig. 10c). These data confirmed that this model is well suited for the specific fate mapping of the *Prrx1*⁺ mesenchymal-like cell population.

To study the fate of these cells in primary tumours, we treated tumour-bearing mice with TAM and collected the melanoma lesions 30 days after treatment. TdTomato⁺ cells were isolated using FACS and the cell composition was analysed using scRNA-seq (Methods and Supplementary Fig. 2). Whereas 8% of the entire tumour population expressed tdTomato in tumours that were collected shortly after TAM exposure (early labelled), this number dropped to about 2% 30 days after TAM treatment (late labelled). Moreover, whereas about 35% of the tdTomato⁺ cells were annotated as malignant at the early time point, this number dropped to about 4% at the late time point (Fig. 4f). These data indicated that the *Prrx1* population does not contribute to the expansion of these primary tumours. Interestingly, although none of the tdTomato⁺ malignant cells expressed the melanocytic program at the early time point, a small number of cells had activated this program at the late time point, indicating that a fraction of the *Prrx1* mesenchymal-like cells (or their progeny) can switch phenotype in primary tumours (Fig. 4g). Notably, a high fraction of disseminated tumour cells in the lymph nodes (late labelled) was found to be tdTomato positive (Extended Data Fig. 10d,e). Whereas a fraction of cells expressed high levels of both GFP and tdTomato in the subcapsular sinuses of lymph nodes, a large fraction of tdTomato⁺ cells that had invaded/expanded in the cortical region expressed lower levels of GFP. Similarly, whereas tdTomato⁺ cells could be identified in the liver and lungs (late labelled), the majority of these cells exhibited low to undetectable GFP expression. The decrease in GFP expression seemed to occur very early during the metastatic cascade. This is, for example,

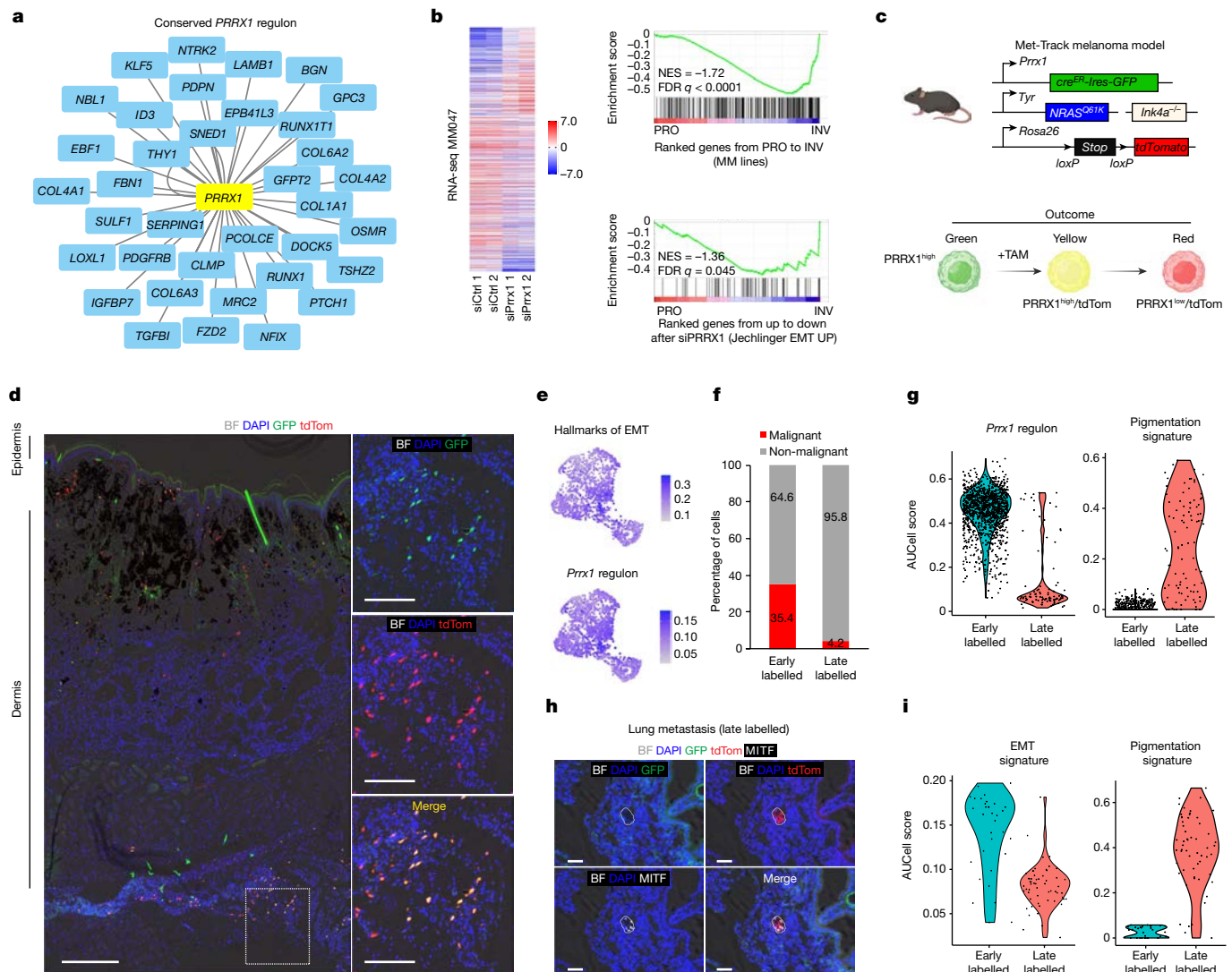


Fig. 4 | Temporal single-cell tracing identified a population of melanoma cells that fuels metastasis but not primary tumour growth. a, The conserved *PRRX1* (human) and *Prrx1* (mouse) regulon (Methods). **b**, Differentially expressed genes after silencing of *PRRX1* in MM047 cells (left) (bulk RNA-seq). $n = 2$ biological replicates. Right, GSEA showing downregulation of the mesenchymal-like signature after treatment with short interfering RNA targeting *PRRX1* (siPRRX1) (MM lines and Jechlinger EMT UP gene sets). **c**, Schematic of the Met-Track mouse model and possible lineage tracing outcomes after TAM exposure. The schematic was created using BioRender. **d**, Confocal images of a primary tumour 4 weeks after TAM treatment. Insets: the majority of GFP⁺tdTomato⁺ (tdTom) double-positive cells are in the deeper dermal part of the lesion. BF, bright field. $n = 4$ independent mice. Scale bars, 500 μm (left) and 50 μm (right). **e**, UMAP analysis showing hallmarks of EMT and *PRRX1* regulon activity (AUCCell score;

colour scales) in tdTomato⁺ cells 2 days (early labelled) after treatment with TAM. **f**, The ratio of malignant versus non-malignant (as determined using scRNA-seq) in the FACS-sorted tdTomato⁺ fraction from primary tumours 2 days (early labelled) and 30 days (late labelled) after treatment with TAM. **g**, Expression of the *PRRX1* regulon and pigmentation signatures (determined using scRNA-seq) in the FACS-sorted tdTomato⁺ fraction from primary tumours 2 days (early labelled) and 30 days (late labelled) after last TAM administration. **h**, Confocal images of a lung micrometastasis 4 weeks after treatment with TAM, immunostained for MITF (white). Red, tdTomato expression; green, GFP. $n = 3$ independent mice. Scale bars, 50 μm . **i**, Expression of the *PRRX1* regulon and pigmentation gene signatures (as determined using scRNA-seq) in the FACS-sorted tdTomato⁺ fraction from lung metastatic lesions 2 days (early labelled) and 30 days (late labelled) after treatment with TAM.

illustrated by the low to undetectable GFP signal in a lung micrometastasis or in disseminated tdTomato⁺ melanoma cells that infiltrated the liver of one of the MetTrack mice (Fig. 4h and Extended Data Fig. 10f).

To further study cell-fate dynamics during metastatic dissemination, we isolated early- and late-labelled tdTomato⁺ cells from the lungs of TAM-treated mice, and the cell composition was analysed using scRNA-seq (Methods and Supplementary Fig. 2). Cells from the early-labelled lungs expressed the EMT/mesenchymal-like signature, but undetectable to very low levels of *Mitf* and the MITF-driven pigmentation signature (Fig. 4i and Extended Data Fig. 10g). By contrast, whereas expression of *Mitf* and other pigmentation markers could be

detected in cells isolated from late-labelled lungs, these cells did not express high levels of the EMT/mesenchymal-signature. High levels of MITF expression in these cells was confirmed by immunohistochemistry analysis (Fig. 4h). This longitudinal analysis indicated that *Prrx1* marks a population that does not contribute to primary tumour growth but, instead, forms a pool of metastatic initiating cells.

Discussion

Here we show that the growth of melanoma is supported by a relatively limited population of tumorigenic cells and provide several lines of

evidence indicating that a dedifferentiated melanoma cell population that exhibits an embryonic transcriptional program activated in cells at the origin of the embryonic NC stem cell lineage may sit at the apex of this cellular hierarchy. Notably, the non-random spatial distribution of these cells, which we found were enriched at the tumour vasculature, raised the possibility that their tumour-fuelling ability may be acquired through exposure to specific extrinsic cues, such as signals emanating from the endothelium, rather than driven by an intrinsic cancer stem cell program. Consistent with this possibility, we show that ECs stimulate melanoma dedifferentiation and promote the *in vitro* and *in vivo* growth of melanoma in a manner that is dependent on NOTCH3—a receptor that is expressed specifically in the pre-EMT NC stem-like population. These data therefore support a dynamic model of hierarchical growth in which dedifferentiation can serve as a source of cancer stem cells. This permutable cancer stem cell paradigm may help to reconcile evidence supporting the scarcity of melanoma cells with high tumorigenic potential^{38–40} with apparently conflicting reports showing that a large fraction of melanoma cells can exhibit tumorigenic potential in xenotransplantation experiments^{40,41}.

Consistent with a model in which tumour growth is supported by a limited population of tumorigenic cells, lineage-tracing analysis of the mesenchymal-like melanoma cell state indicated that these cells do not contribute to the expansion of primary tumours but, instead, constitute a pool of metastatic initiating cells. We identified *Prrx1* as a marker of this state and we generated a mouse model, named Met-Track, that enables the fate mapping of this *Prrx1*⁺ MIC population. Temporal single-cell tracing revealed that a large fraction of metastatic initiating cells (and/or their progeny) change cell identity when (or even before) reaching their metastatic sites. This suggests that metastatic outgrowth can occur only after suppression of the *Prrx1*⁺ mesenchymal-like transcriptional program. Such a reprogramming event is reminiscent of the mesenchymal-to-epithelial transition process described in epithelial cancers⁴². These data are consistent with previous findings showing that PRRX1 promotes EMT while suppressing stemness traits in breast cancer cells³³.

In conclusion, our study provides a high-resolution and spatially resolved map of the mouse melanoma ecosystem, charting the origin of phenotypic diversity and tumour growth. Together with the Met-Track mouse model we report here, these resources provide a platform to study extrinsic and systemic factors driving primary tumour growth and metastatic dissemination, with the potential to develop methods for early detection, as well as therapeutic strategies that intercept the disease before its spreading to vital organs.

Online content

Any methods, additional references, Nature Research reporting summaries, source data, extended data, supplementary information, acknowledgements, peer review information; details of author contributions and competing interests; and statements of data and code availability are available at <https://doi.org/10.1038/s41586-022-05242-7>.

- Rambow, F., Marine, J. C. & Goding, C. R. Melanoma plasticity and phenotypic diversity: therapeutic barriers and opportunities. *Genes Dev.* **33**, 1295–1318 (2019).
- Arozarena, I. & Wellbrock, C. Phenotype plasticity as enabler of melanoma progression and therapy resistance. *Nat. Rev. Cancer* **19**, 377–391 (2019).
- Gulati, G. S. et al. Single-cell transcriptional diversity is a hallmark of developmental potential. *Science* **367**, 405–411 (2020).
- Rambow, F. et al. Toward minimal residual disease-directed therapy in melanoma. *Cell* **174**, 843–855 (2018).
- Tirosh, I. et al. Dissecting the multicellular ecosystem of metastatic melanoma by single-cell RNA-seq. *Science* **352**, 189–196 (2016).
- Wouters, J. et al. Robust gene expression programs underlie recurrent cell states and phenotype switching in melanoma. *Nat. Cell Biol.* **22**, 986–998 (2020).
- Patton, E. E. et al. Melanoma models for the next generation of therapies. *Cancer Cell* **39**, 610–631 (2021).

- Ackermann, J. et al. Metastasizing melanoma formation caused by expression of activated N-Ras^{G61K} on an INK4a-deficient background. *Cancer Res.* **65**, 4005–4011 (2005).
- Serrano, M. et al. Role of the INK4a locus in tumor suppression and cell mortality. *Cell* **85**, 27–37 (1996).
- Tirosh, I. et al. Dissecting the multicellular ecosystem of metastatic melanoma by single-cell RNA-seq. *Science* **352**, 189–196 (2016).
- Jerby-Arnon, L. et al. A cancer cell program promotes T cell exclusion and resistance to checkpoint blockade. *Cell* **175**, 984–997 (2018).
- Rambow, F. et al. New functional signatures for understanding melanoma biology from tumor cell lineage-specific analysis. *Cell Rep.* **13**, 840–853 (2015).
- Sade-Feldman, M. et al. Defining T cell states associated with response to checkpoint immunotherapy in melanoma. *Cell* **175**, 998–1013 (2018).
- Fan, J. et al. Linking transcriptional and genetic tumor heterogeneity through allele analysis of single-cell RNA-seq data. *Genome Research* **28**, 1217–1227 (2018).
- Goding, C. R. & Arnheiter, H. MITF—the first 25 years. *Genes Dev.* **33**, 983–1007 (2019).
- Hoek, K. S. & Goding, C. R. Cancer stem cells versus phenotype-switching in melanoma. *Pigment Cell Melanoma Res.* **23**, 746–759 (2010).
- Aibar, S. et al. SCENIC: single-cell regulatory network inference and clustering. *Nat. Methods* **14**, 1083–1086 (2017).
- Soldatov, R. et al. Spatiotemporal structure of cell fate decisions in murine neural crest. *Science* **364**, eaas9536 (2019).
- Kerosuo, L. & Bronner, M. E. cMyc regulates the size of the premigratory neural crest stem cell pool. *Cell Rep.* **17**, 2648–2659 (2016).
- Tsoi, J. et al. Multi-stage differentiation defines melanoma subtypes with differential vulnerability to drug-induced iron-dependent oxidative stress. *Cancer Cell* **33**, 890–904 (2018).
- Köhler, C. et al. Mouse cutaneous melanoma induced by mutant BRAF arises from expansion and dedifferentiation of mature pigmented melanocytes. *Cell Stem Cell* **21**, 679–693 (2017).
- Pozniak, J. et al. A TCF4/BRD4-dependent regulatory network confers cross-resistance to targeted and immune checkpoint therapy in melanoma. Preprint at *bioRxiv* <https://doi.org/10.1101/2022.08.11.502598> (2022).
- Snippert, H. J. et al. Intestinal crypt homeostasis results from neutral competition between symmetrically dividing Lgr5 stem cells. *Cell* **143**, 134–144 (2010).
- Reeves, M. Q., Kandyba, E., Harris, S., Del Rosario, R. & Balmain, A. Multicolour lineage tracing reveals clonal dynamics of squamous carcinoma evolution from initiation to metastasis. *Nat. Cell Biol.* **20**, 699–709 (2018).
- Stuart, T. et al. Comprehensive integration of single-cell data. *Cell* **177**, 1888–1902 (2019).
- Chen, A. et al. Spatiotemporal transcriptomic atlas of mouse organogenesis using DNA nanoball-patterned arrays. *Cell* **185**, 1777–1792 (2022).
- Calabrese, C. et al. A perivascular niche for brain tumor stem cells. *Cancer Cell* **11**, 69–82 (2007).
- Browaeys, R., Saelens, W. & Saeys, Y. NicheNet: modeling intercellular communication by linking ligands to target genes. *Nat. Methods* **17**, 159–162 (2020).
- Jin, S. et al. Inference and analysis of cell-cell communication using CellChat. *Nat. Commun.* **12**, 1088 (2021).
- Subramanian, A. et al. Gene set enrichment analysis: a knowledge-based approach for interpreting genome-wide expression profiles. *Proc. Natl Acad. Sci. USA* **102**, 15545–15550 (2005).
- Wei, K. et al. Notch signalling drives synovial fibroblast identity and arthritis pathology. *Nature* **582**, 259–264 (2020).
- Takano, S. et al. *Prrx1* isoform switching regulates pancreatic cancer invasion and metastatic colonization. *Genes Dev.* **30**, 233–247 (2016).
- Ocaña, O. H. et al. Metastatic colonization requires the repression of the epithelial-mesenchymal transition inducer *Prrx1*. *Cancer Cell* **22**, 709–724 (2012).
- Hoek, K. S. et al. *In vivo* switching of human melanoma cells between proliferative and invasive states. *Cancer Res.* **68**, 650–656 (2008).
- Verfaillie, A. et al. Decoding the regulatory landscape of melanoma reveals TEADs as regulators of the invasive cell state. *Nat. Commun.* <https://doi.org/10.1038/ncomms7683> (2015).
- Widmer, D. S. et al. Systematic classification of melanoma cells by phenotype-specific gene expression mapping. *Pigment Cell Melanoma Res.* **25**, 343–353 (2012).
- Kawanami, A., Matsushita, T., Chan, Y. Y. & Murakami, S. Mice expressing GFP and CreER in osteochondro progenitor cells in the periosteum. *Biochem. Biophys. Res. Commun.* **386**, 477–482 (2009).
- Boiko, A. D. et al. Human melanoma-initiating cells express neural crest nerve growth factor receptor CD271. *Nature* **466**, 133–137 (2010).
- Roesch, A. et al. A temporarily distinct subpopulation of slow-cycling melanoma cells is required for continuous tumor growth. *Cell* **141**, 583–594 (2010).
- Schatton, T. et al. Identification of cells initiating human melanomas. *Nature* **451**, 345–349 (2008).
- Quintana, E. et al. Efficient tumour formation by single human melanoma cells. *Nature* **456**, 593–598 (2008).
- Stemmler, M. P., Eccles, R. L., Brabletz, S. & Brabletz, T. Non-redundant functions of EMT transcription factors. *Nat. Cell Biol.* **21**, 102–112 (2019).

Publisher's note Springer Nature remains neutral with regard to jurisdictional claims in published maps and institutional affiliations.

Springer Nature or its licensor holds exclusive rights to this article under a publishing agreement with the author(s) or other rightsholder(s); author self-archiving of the accepted manuscript version of this article is solely governed by the terms of such publishing agreement and applicable law.

© The Author(s), under exclusive licence to Springer Nature Limited 2022, corrected publication 2022

¹Laboratory for Molecular Cancer Biology, Center for Cancer Biology, VIB, Leuven, Belgium.

²Department of Oncology, KU Leuven, Leuven, Belgium. ³Department of Applied Mathematics and Theoretical Physics, Centre for Mathematical Sciences, University of Cambridge, Cambridge, UK. ⁴The Wellcome Trust/CRUK Gurdon Institute, University of Cambridge, Cambridge, UK. ⁵Department of General Medical Oncology, UZ Leuven, Leuven, Belgium. ⁶BGI-Shenzhen, Shenzhen, China. ⁷VIB Biomedicine Core, VIB Center for Brain and Disease Research, Leuven, Belgium. ⁸VIB Bioimaging Core, VIB Center for Inflammation Research, Ghent, Belgium. ⁹Department of Biomedical Molecular Biology, Ghent University, Ghent, Belgium. ¹⁰FACS Expertise Center, Center for Cancer Biology, VIB, Leuven, Belgium.

¹¹Laboratory of Tumor Microenvironment and Therapeutic Resistance, Center for Cancer Biology, VIB, Leuven, Belgium. ¹²Center for Brain & Disease Research, VIB-KU Leuven, Leuven, Belgium. ¹³Department of Human Genetics, KU Leuven, Leuven, Belgium. ¹⁴Data Mining and Modeling for Biomedicine Group, VIB Center for Inflammation Research, Ghent, Belgium. ¹⁵Department of Applied Mathematics, Computer Science and Statistics, Ghent

University, Ghent, Belgium. ¹⁶Laboratory for Translational Cell and Tissue Research, Department of Imaging and Pathology, KU Leuven, Leuven, Belgium. ¹⁷Laboratory of Translational Genetics, Center for Cancer Biology, VIB, Leuven, Belgium. ¹⁸Laboratory of Translational Genetics, Center for Human Genetics, KU Leuven, Leuven, Belgium. ¹⁹Herbert Irving Comprehensive Center, Columbia University Irving Medical Center, New York, USA.

²⁰Laboratory of Stem Cells and Cancer, Université Libre de Bruxelles (ULB), Brussels, Belgium. ²¹Wellcome Trust-MRC Stem Cell Institute, University of Cambridge, Cambridge, UK. ²²Present address: Departamento de Física, Facultad de Ciencias Físicas y Matemáticas, Universidad de Chile, Santiago, Chile. ²³Department of Applied Computational Cancer Research, Institute for AI in Medicine (IKIM), University Hospital Essen, Essen, Germany.

²⁴University Duisburg-Essen, Essen, Germany. ²⁵German Cancer Consortium (DKTK), partner site Essen, Essen, Germany. ²⁶These authors contributed equally: Ignacio Bordeu, Joanna Pozniak, Ada Nowosad. [✉]e-mail: florian.rambow@kuleuven.vib.be; jeanchristophe.marine@kuleuven.vib.be

Methods

Compliance with ethical regulations

All of the mouse colonies were maintained in a certified animal facility in accordance with European guidelines. Specifically, animals were housed in a controlled environment under 14 h–10 h light–dark cycles, standard diet and water ad libitum. All of the experiments strictly complied with the protocols approved by the University of Leuven Animal Care and Use ethical committee. Mice were euthanized at different time points and tumour sizes or if the tumour was ulcerated independently of its size, if the mouse lost >20% of the initial weight or showed any other sign of distress (based on the general health status). None of the experiments performed in this study surpassed the size limit of the tumours (the volume did not exceed 2 cm³). No randomization and blinding were performed in this study.

Mice

We intercrossed the following strains: *Tyr::cre^{ERT2}* (ref. 43), *Tyr::NRAS^{Q61K}* (ref. 8), *Ink4a^{-/-}* (ref. 44), *Rosa26R^{LSL-tdTomato}* (Jackson laboratory, 007909), *Rosa26R^{LSL-confetti}* (ref. 23), *Braf^{CA/+}* (ref. 45), *Pten^{fl/fl}* (ref. 45) and *Prrx1::cre^{ER}-Ires2-EGFP³⁷* to generate *Tyr::cre^{ERT2/+};NRAS^{Q61K/+};Ink4a^{-/-};Rosa26R^{LSL-confetti/LSL-confetti}*, *Tyr::cre^{ERT2/+};Braf^{CA/+};Pten^{fl/fl};Rosa26R^{LSL-tdTomato/LSL-tdTomato}* and *Prrx1::cre^{ER}-GFP;Tyr-NRAS^{Q61K/+};Ink4a^{-/-};Rosa26R^{LSL-tdTomato/LSL-tdTomato}* compound mice.

For the generation of the melanoma allograft models, spontaneous skin melanoma lesions from *Tyr::cre^{ERT2/+};Tyr-NRAS^{Q61K/+};Ink4a^{-/-};Rosa26R^{LSL-confetti/LSL-confetti}* animals were dissociated into small pieces using forceps and scissors. Some of these tumour pieces were subcutaneously engrafted into C57BL/6 or *Foxn1^{nu/nu}* mice and expanded for three generations before starting the clonal analyses. Tumour volume was monitored using callipers and the volume was calculated using the following formula: $V = (\pi/6) \times \text{length} \times \text{width} \times \text{height}$.

For lineage-tracing experiments, TAM (Sigma-Aldrich, T5648) was dissolved in 10% ethanol and 90% corn oil for 4 h at 55 °C. Aliquots were kept at -20 °C. Stock solutions of 5 mg ml⁻¹ and 20 mg ml⁻¹ were prepared and 100 µl was administered intraperitoneally. For the clonal analysis on the Confetti background, the dose of TAM was titrated down up to 0.5 mg ml⁻¹. The mice were injected once their tumours reached an approximate volume of 150 mm³ and were euthanized at the indicated time points after injections or just before the tumours reached the humane end point. The *Prrx1::cre^{ER}-GFP;Tyr-NRAS^{Q61K/+};Ink4a^{-/-};Rosa26R^{LSL-tdTomato/LSL-tdTomato}* mice were induced by intraperitoneal injection of 2 mg of TAM for 5 consecutive days when primary melanoma lesions had reached an approximate size of 50 mm³. Mice were euthanized either 2 days or 30 days after induction. For tumour induction in the *Tyr::cre^{ERT2};Braf^{V600E/+};Pten^{fl/fl}* tail mouse model, mice (aged 6 weeks) were topically treated with 130 mM of 4-hydroxy-tamoxifen using 1 µl per cm (tail length) and euthanized 111 days after treatment. To induce the formation of the back-skin tumours, mice were topically treated on the back with 1 µl of 130 mM 4-hydroxy-tamoxifen and euthanized 65 days after treatment.

For the proliferation kinetics experiments, the mice were first intraperitoneally injected daily for 9 consecutive days with EdU (25 mg kg⁻¹ in PBS, Invitrogen, E10415) and then daily for 3 consecutive days with BrdU (50 mg kg⁻¹ in PBS, Sigma-Aldrich, 19-160). The mice were euthanized 24 h after the last BrdU injection.

Co-injection of melanoma and ECs in mice

Tyr::NRAS^{Q61K/+};Ink4a^{-/-} mouse melanoma cells stably expressing dsRed-encoding lentiviruses and bEnd.3 ECs (ATCC, CRL-2299) stably expressing GFP encoding lentiviruses were mixed at a ratio of 1:2 (10⁵ melanoma cells:2 × 10⁵ ECs) and 1:4 (10⁵ melanoma cells:4 × 10⁵ ECs) and resuspended in Matrigel (5 mg ml⁻¹; Thermo Fisher Scientific, 356255). Cells were then injected subcutaneously in the back skin of *Foxn1^{nu}* mice. The mice were euthanized and tumours were collected 25 days after melanoma initiation. To measure overall survival, tumours were grown

until reaching a humane end point of approximately 1.5 cm³. Tumour volume was monitored with callipers and the volume was calculated using the following formula: $V = (\pi/6) \times \text{length} \times \text{width} \times \text{height}$.

Immunofluorescence of mouse frozen tissue sections

Tissue samples were dissected and fixed for 20 min in 4% paraformaldehyde at room temperature. The samples were washed in PBS and incubated overnight in 30% sucrose in PBS at 4 °C. Tissue samples were then embedded in Tissue-Tek O.C.T. Compound (Sakura Finetek, 4583) and stored at -80 °C. Sections of 10 µm were cut using the Thermo Fisher Scientific CryoStar NX70 Cryostat. For immunofluorescence, tissue sections were fixed for 10 min in 4% paraformaldehyde on ice. Sections were washed in PBS for 5 min at room temperature, permeabilized in 1% Triton X-100 in PBS for 10 min at room temperature and washed in 0.1% Tween-20 (VWR chemicals, Amresco, 0777) in TBS. The sections were incubated in blocking buffer (1% BSA, 10% donkey serum, 0.1% Tween-20 in TBS) for 1 h at room temperature. Subsequently, primary antibodies were incubated overnight at 4 °C in antibody diluent (1% BSA, 0.1% Tween-20 in TBS). The sections were washed three times using 0.1% Tween-20 in TBS for 5 min at room temperature and incubated with the corresponding secondary antibodies diluted 1:250 in antibody diluent for 1 h at room temperature. Sections were washed three times for 5 min at room temperature, nuclei were stained with 4',6-diamino-2-phenylindole (DAPI, dihydrochloride, 1:1,000 dilution, Thermo Fisher Scientific, D3571) solution (0.5 mg ml⁻¹) diluted 1:1,000 in PBS for 5 min and mounted in ProLong Diamond Antifade Mountant (Thermo Fisher Scientific, P36961).

For EdU and BrdU staining, the samples were first stained with the primary antibody, and then washed and stained with the secondary antibody, as described above. To denature the DNA, the sections were incubated in 2 N HCl for 30 min at 37 °C and the acid was neutralized by immersing the sections in 0.1 M borate buffer twice for 5 min. The sections were washed three times using 0.1% Tween-20 in TBS for 5 min and incubated overnight with BrdU antibody in blocking buffer. The next day, the samples were washed in 0.1% Tween-20 in TBS and incubated with secondary antibody. The samples were washed three times in 0.1% Tween-20 in TBS and proceeded for EdU detection. Edu staining was performed using the Click-iT EdU Cell Proliferation Kit for Imaging with Alexa Fluor 647 dye according to the manufacturer's instructions (Thermo Fisher Scientific, C10340).

The following primary antibodies were used: anti-GP100 (1:400, Abcam, ab137078); anti-MITF (rabbit, 1:200, Sigma-Aldrich, HPA003259); anti-AQP1 (1:2,000, Millipore, AB2219); anti-CD31/PECAM-1 (1:200, Dianova, DIA-310); anti-MLANA (1:200, Sigma-Aldrich, HPA048662), anti-NES (1:100, Abcam, ab81462) and anti-BrdU (1:100, Abcam, ab6326). The following secondary antibodies were used: donkey-anti-rat IgG (H+L), Alexa Fluor 488 (Thermo Fisher Scientific, A-21208); donkey-anti-rabbit IgG (H+L), Alexa Fluor 647 (Thermo Fisher Scientific, A31573) and goat-anti-rat IgG (H+L), Alexa Fluor 647 (Thermo Fisher Scientific, A21247).

Histopathology analysis of mouse tissue specimens

Tissue samples were collected and fixed in 4% paraformaldehyde for 24 h and processed for paraffin embedding (Thermo Fisher Scientific Excelsior AS Tissue Processor and HistoStar Embedding Workstation). Sections (thickness, 5 µm) were obtained from the paraffin-embedded tissues (Thermo Fisher Scientific Microm HM355S microtome) and mounted onto Superfrost Plus Adhesion slides (Thermo Fisher Scientific) and stained with haematoxylin and eosin (H&E, Diapath, C0302 and C0362) for histopathological examination.

Immunofluorescence analysis of mouse paraffin-embedded tissue specimens

We used the opal-based approach, which relies on individual tyramide signal amplification (TSA)-conjugated fluorophores to detect various targets. After deparaffinization, antigen retrieval was performed in

Article

citrate buffer at pH 6. The sections were incubated for 2 h (room temperature) or overnight (4 °C) with the following primary antibodies: anti-AQP1 (1:2,000, Millipore, AB2219), anti-SOX10 (1:100, Thermo Fisher Scientific, 703439), anti-NOTCH3 (1:100, Abcam, ab23426). The slides were then washed and incubated for 5 min with successive washes in TBST at room temperature. The slides were next incubated at room temperature for 10 min with one of the following Alexa Fluor tyramides (PerkinElmer) to detect antibody staining, prepared according to the manufacturer's instructions: Opal 520, Opal 570 and Opal 690 (dilution 1:50). Stripping of primary and secondary antibodies was performed by placing the slides into a plastic container filled with antigen retrieval (AR) buffer in citrate buffer pH 6. A microwave was used to heat the liquid to 100 °C (2 min), and the sections were then microwaved for an additional 15 min at 75 °C. Slides were allowed to cool down in the AR buffer for 15 min at room temperature and were then rinsed with deionized water and 1× Tris-buffered saline with Tween-20. After three additional washes in deionized water, the slides were counterstained with DAPI for 5 min and mounted with ProLong Gold Antifade Mountant (Thermo Fisher Scientific, P36930).

Immunofluorescence analysis of human biopsies

Sections (5 µm) of formalin-fixed, paraffin-embedded primary nodal melanoma lesions were stained with antibodies against SOX10 (SCBT, sc-365692; 1 µg ml⁻¹), VCAN (Sigma-Aldrich, HPA004726; 0.2 µg ml⁻¹) and CD31 (LSBio, LS-C173974; 1 µg ml⁻¹) according to the Multiple Iterative Labelling by Antibody Neodeposition (MILAN) protocol⁴⁶. Image registration was performed by applying a homomorphic transformation over a set of matched descriptors using a Harris detector. Autofluorescence (AF) subtraction was performed by subtracting the scaled AF channel from the measured signal (MS). The scaling factor was obtained by applying Gaussian mixture models and linear modelling in the MS/AF hypermatrix. For SOX10/NES double-positive cells, opal-based immunofluorescence was used in primary human biopsies as described above. The sections were incubated at 2 h (at room temperature) or overnight (4 °C) with the following primary antibodies: anti-AQP1 (1:2,000, Millipore, AB2219), anti-SOX10 (1:200, R&D Systems, AF2864) and anti-NES (1:100, Abcam, ab105389).

Tissue clearing

Tissue clearing was performed using a protocol described previously⁴⁷ with modifications. Tumour pieces from an allograft melanoma model of approximately 1 mm thickness were fixed overnight in 4% PFA at 4 °C. The samples were washed three times in PBS and cleared using a modified protocol of CUBIC (Clear, Unobstructed Brain Imaging Cocktails and Computational analysis). In brief, Sca/eCUBIC-1 (reagent 1A) was prepared as a mixture of 10 wt% urea (Nacalai Tesque, 35904-45), 5 wt% N,N,N',N'-tetrakis(2-hydroxypropyl) ethylenediamine (Tokyo Chemical Industry, T0781), 10 wt% Triton X-100 (Nacalai Tesque, 25987-85) in 5 M NaCl. Sca/eCUBIC-2 (reagent 2) was prepared as a mixture of 50 wt% sucrose (Nacalai Tesque, 30403-55), 25 wt% urea, 10 wt% 2,2,0,2'-nitrioltriethanol (Wako Pure Chemical Industries, 145-05605), 0.1% (v/v) Triton X-100 and 0.1% (v/v) sodium azide. Tumour pieces were incubated in 1/2-diluted reagent-1A for 6 h at room temperature with shaking. The samples were then incubated in reagent-1A at room temperature for 2 days on a rocking plate (100 rpm) protected from the light. The samples then were moved at 37 °C under continuous shaking with fresh medium that was replaced every second day. After 8 days, the samples were washed with PBS and immersed in 1/2-diluted reagent-2 for at least 24 h at room temperature and then immersed in reagent-2 at room temperature for 2 days. Immunostaining of CUBIC tissue cleared samples to visualize confetti clones in respect to blood vessels (assessed by CD31 positivity) was performed after incubation with reagent-1A. The samples were incubated with primary antibodies (CD31/PECAM-1, 1:200, Dianova, DIA-310) resuspended blocking buffer (PBS with 0.1% TritonX-100 and 10% normal goat serum) for 3 days at

37 °C with rotation. The cleared tumours were then washed several times with washing buffer (PBS with 0.1% Triton X-100) at 37 °C with rotation. Secondary antibody (goat-anti-rat IgG, Alexa Fluor 647, 1/200, Thermo Fisher Scientific, A21247) resuspended in blocking buffer was added and the samples were incubated for 3 days at 37 °C with rotation. Then samples were washed and counterstained with DAPI (1/1,000) for 24 h at 37 °C with rotation. The samples were then immersed in reagent 2 for 2 days. The samples were acquired using the Zeiss LSM 880 Airyscan.

Spatially resolved transcriptomics using Visium

For tissue processing and slide preparation, tumours were dissected, washed with 1× PBS and snap-frozen in liquid-nitrogen-chilled isopentane. The frozen tumours were then transferred to a cold tissue mould filled with chilled OCT. The cryomold was then immediately placed on dry ice. Tissue blocks were stored at -80 °C in a sealed container. For cryosectioning, both the tissue block and the Visium slide were equilibrated inside the cryostat for 30 min at -12 °C before sectioning. Sections were cut at a thickness of 10 µm and immediately placed onto the Visium array slide (Visium Spatial Gene Expression slides, 10x Genomics). Array slides containing sections were stored at -80 °C for 24 h before use.

For fixation, staining, imaging and construction of cDNA libraries, samples were processed according to the manufacturer's instructions (Visium Spatial Gene Expression User Guide, Rev. 10x Genomics) and all of the reagents were from the Visium Spatial Gene Expression Kit (10x Genomics). In brief, sections were fixed in chilled methanol for 30 min at -20 °C and stained with H&E. Imaging was performed on the Nikon-Marzhauser Slide Express 2 whole-slide scanner at ×20 magnification. After imaging, the sections were permeabilized at 37 °C for 20 min. The permeabilization time was determined using the Visium Spatial Tissue Optimization Kit (10x Genomics). After permeabilization, the on-slide reverse transcription reaction was performed at 53 °C for 45 min. Second-strand synthesis was subsequently performed on-slide for 15 min at 65 °C. All on-slide reactions were performed in a thermocycler with a metal slide adapter plate. After second-strand synthesis, the samples were transferred to tubes for cDNA amplification and clean-up. Cycle number determination for cDNA amplification was done by quantitative PCR (qPCR) according to the manufacturer's instructions. Library quality control was accessed using a TapeStation (Agilent).

Visium libraries were sequenced on the Illumina NovaSeq 6000 instrument (parameters: SP flowcell 100 cycles single reads, lane 1 = 220 pM + 1% PhiX/lane 2 = 215 pM + 1% PhiX). We obtained 998 million raw passed filter reads. BCL2 sequencing files were further processed using SpaceRanger (v.1.0.0, 10x Genomics) to generate spatial gene expression matrices. In parallel, we performed manual grid-alignment using the loupe browser (v.4.2.0, 10x Genomics). The SpaceRanger output of the three melanoma samples was further analysed using the Seurat spatial vignette (<https://satijalab.org/seurat/vignettes.html>). In brief, spots were retained when $n_{\text{Feature_Spatial}} > 1,000$ and $\text{percent.mt} < 5$ and expression data were normalized using SCTransform (Seurat, v.3.2.3)²⁵. The spatial distribution of the different transcriptional melanoma states was inferred using CCA-based label transfer ($k_{\text{anchor}} = 10$). The resulting prediction scores (0.0–1.0) for the different melanoma states were further used to correlate the distance of every spot to the nearest vessel. To do so, vessels that were identified by the pathologist based on matching HE-stained sections were manually selected using the Loupe browser (10x Genomics). The Euclidean distance between all spots was then calculated and returned for each spot a distance to the nearest vessel-annotated spot. For Spearman correlation, stress-like (hypoxia) prediction scores per spot had to be greater than or equal to 0.008 and each spot had to contain at least $n = 10$ reads for *Sox10*. This resulted in $n = 263$ spots for all 3 samples. For putative pre-EMT NC stem-like spots, the pre-EMT NC stem-like prediction score had to be greater than or equal to 0.04, spots needed to be *Sox10* positive and negative for *Rgs5*. This resulted in 626 pre-EMT NC stem-like spots that were correlated with 'distance to the nearest vessel'.

Spatial transcriptomics using stereo-seq

Stereo-seq chips have DNA nanoball (DNB) bins with a 220 nm diameter and a centre-to-centre distance of 500 nm. For sample preparation and sequencing, tissue blocks in OCT (Sakura, 4583) were cut into sections of 10 μm thickness using a cryostat (Leica, CM1950) and adhered to the stereo-seq chip surface (BGI Research) to generate a cDNA library as described previously²⁶. In brief, a 10 μm tissue section was adhered to the surface of the stereo-seq chip, whereas the adjacent sections were used for H&E staining or immunohistochemistry. The chip was placed onto a warming plate (Bel-Art, BELAF370151000) at 37 °C for 3 min to dry and immersed in precooled methanol at -20 °C for 30 min for fixation. The chip was incubated with 100 μl 0.1% pepsin (Sigma-Aldrich, P7000) at 37 °C for 12 min and washed with 0.1 \times SSC buffer (Thermo Fisher Scientific, AM9770) containing 0.05 U μl^{-1} RNase inhibitor. RNA released from the permeabilized tissue was captured by DNB on the chip and reverse-transcribed using 100 μl SuperScript reverse transcription II mix (10 U μl^{-1} reverse transcriptase, 1 mM dNTPs, 1 M betaine solution PCR reagent, 7.5 mM MgCl₂, 5 mM DTT, 2 U μl^{-1} RNase inhibitor, 2.5 μM stereo-seq template switch oligo, and 1 \times first-strand buffer) at 42 °C for 90 min. Tissue on the chip was removed by incubating with tissue removal buffer (10 mM Tris-HCl, 25 mM EDTA, 100 mM NaCl, 0.5% SDS) at 55 °C for 10 min. After washing twice with 0.1 \times SSC buffer, the chip was incubated with 400 μl cDNA release buffer at 55 °C for 4 h. The cDNA was then purified using AMPure XP DNA Clean Beads (Vazyme, N411-03) and amplified using KAPA HiFi Hotstart Ready Mix (Roche, KK2602) and cDNA primers. A total of 20 ng of cDNA PCR product was fragmented to generate the cDNA sequencing library. The cDNA library was loaded onto a G400 sequencer (MGI) for sequencing (pair-end, read 1 of 50 bp and read 2 of 100 bp).

For cell-type probability calculations, the probability of a single bin50 matching a specific cell type was measured using the AUCell package (<https://doi.org/10.18129/B9.bioc.AUCell>) with the default parameters. Then, 50 endothelial marker genes, 14 SuperMel markers and the top 100 signature genes for pre-EMT NC stem-like and stress-like (hypoxia) were used (Supplementary Table 6). Bin50 spots within an area of 320 \times 160 bin50 units were selected for further analysis (bin50 resolution, 25 μm diameter). Within the targeted area, the median molecular identifier and gene counts of the bin50 spots were 1,932 and 1,023, respectively. The maximum percentage of mitochondrial genes was 2.8% with an average of 0.84%.

For statistical analysis, correlations between two variables (for example, AUCell values of two cell types) were calculated using the R environment built-in function `cor.test` with the default parameters (Spearman's correlation coefficient). Blood vessels were identified using AUCell binary cut-off and expression of 1 or more EC markers (*Aqp1*, *Gpihbp1*, *Pecam1*, *Kdr* and *Cdh5*). Both pre-EMT NC stem-like and stress-like (hypoxia) spots had to be *Sox10* positive and negative for *Kdr* and *Cdh5*. This resulted in 4,153 spots that were correlated with 'distance to nearest vessel'.

Molecular Cartography

To prepare tissue sections, tumour samples were resected and fixed for 24 h in PAXgene tissue fix after incubation for 2 h with PAXgene Tissue Stabilizer. Three sections from two tumour samples were used. Sections (thickness, 10 μm) were placed within the capture areas of cold Resolve Biosciences slides, thawed and treated with isopropanol for 1 min followed by 1 min washes in 95% ethanol and 70% ethanol at room temperature. The samples were used for Molecular Cartography (100-plex combinatorial single-molecule fluorescence in situ hybridization) according to the manufacturer's instructions (protocol 4.0; available for download from Resolve's website to registered users), starting with the aspiration of ethanol and the addition of buffer BST1 (step 6 and 7 of the tissue priming protocol). In brief, tissues were primed followed by overnight hybridization of all probes specific for the target genes (the probe design details

and target list are provided below). The samples were washed the next day to remove excess probes and were then fluorescently tagged in a two-step colour development process. ROIs were imaged as described below and fluorescence signals were removed during decolourization. Colour development, imaging and decolourization were repeated for multiple cycles to build a unique combinatorial code for every target gene that was derived from raw images as described below.

For the probe design of the 97 selected genes, we used the Resolve's proprietary design algorithm. For every targeted gene, the full-length protein-coding transcript sequence from the ENSEMBL database was used as design target if the isoform had the GENCODE annotation tag 'basic'^{48,49}. To filter highly repetitive regions, the abundance of k -mers was obtained from the background transcriptome using Jellyfish⁵⁰. Every target sequence was scanned once for all k -mers, and those regions with rare k -mers were preferred as seeds for full probe design. A probe candidate was generated by extending a seed sequence until a certain target stability was reached. A set of simple rules was applied to discard sequences that were previously found to cause problems experimentally. After these fast screens, every selected probe candidate was mapped to the background transcriptome using ThernucleotideBLAST⁵¹ and probes with stable off-target hits were discarded. Specific probes were then scored on the basis of the number of on-target matches (isoforms), which were weighted by their associated APPRIS level⁵², favouring principal isoforms over others. A bonus was added if the binding site was inside the protein-coding region. From the pool of accepted probes, the final set was composed by greedily picking the highest scoring probes (Supplementary Table 7).

A total of 33 ROIs of all samples were imaged on a Zeiss CellDiscoverer 7, using the $\times 50$ plan apochromat water-immersion objective with an NA of 1.2 and a $\times 0.5$ magnification changer, resulting in a $\times 25$ final magnification. A standard CD7 LED excitation light source, filters and dichroic mirrors were used together with customized emission filters optimized for detecting specific signals. The excitation time per image was 1,000 ms for each channel (DAPI was 20 ms). A z -stack was taken at each region with a distance per z -slice according to the Nyquist-Shannon sampling theorem. The custom CD7 CMOS camera (Zeiss AxioCam Mono 712, 3.45 μm pixel size) was used. For each region, a z -stack per fluorescent colour (two colours) was imaged per imaging round. A total of 8 imaging rounds were performed for each position, resulting in 16 z -stacks per region. The completely automated imaging process per round (including water-immersion generation and precise relocation of the regions to image in all three dimensions) was realized using a custom Python script using the scripting API of the Zeiss ZEN software (open application development).

For spot segmentation, the algorithms for spot segmentation were written in Java and are based on the ImageJ library functionalities. Only the iterative closest point algorithm is written in C++ based on the libpointmatcher library (<https://github.com/ethz-asl/libpointmatcher>).

For preprocessing, as a first step, all of the images were corrected for background fluorescence. A target value for the allowed number of maxima was determined on the basis of the area of the slice in μm^2 multiplied by the factor 0.5. This factor was empirically optimized. The brightest maxima per plane were determined based on an empirically optimized threshold. The number and location of the respective maxima was stored. This procedure was performed for every image slice independently. Maxima that did not have a neighbouring maximum in an adjacent slice (called z -group) were excluded. The resulting maxima list was further filtered in an iterative loop by adjusting the allowed thresholds for $(B_{\text{abs}} - B_{\text{back}})$ and $(B_{\text{peri}} - B_{\text{back}})$ to reach a feature target value, where B_{abs} is the absolute brightness, B_{back} is the local background and B_{peri} is the background of periphery within 1 pixel). These feature target values were based on the volume of the 3D image. Only maxima still in a z -group of at least 2 after filtering passed the filter step. Each z -group was counted as one hit. The members of the z -groups with the highest absolute brightness were used as features and written to a

Article

file. They resemble a 3D point cloud. For final signal segmentation and decoding, to align the raw data images from different imaging rounds, images had to be corrected. To do so, the extracted feature point clouds were used to find the transformation matrices. For this purpose, an iterative closest-point cloud algorithm was used to minimize the error between two point clouds. The point clouds of each round were aligned to the point cloud of round one (reference point cloud). The corresponding point clouds were stored for downstream processes. On the basis of the transformation matrices, the corresponding images were processed by a rigid transformation using trilinear interpolation. The aligned images were used to create a profile for each pixel consisting of 16 values (16 images from two colour channels in 8 imaging rounds). The pixel profiles were filtered for variance from zero normalized to the total brightness of all of the pixels in the profile. Matched pixel profiles with the highest score were assigned as an ID to the pixel. Pixels with neighbours with the same ID were grouped. The pixel groups were filtered by group size, number of direct adjacent pixels in group, number of dimensions with size of two pixels. The local 3D maxima of the groups were determined as potential final transcript locations. Maxima were filtered by the number of maxima in the raw data images where a maximum was expected. The remaining maxima were further evaluated by the fit to the corresponding code. The remaining maxima were written to the results file and were considered to resemble transcripts of the corresponding gene. The ratios of signals matching to codes used in the experiment and signals matching to codes not used in the experiment were used as an estimation for specificity (false positives).

For downstream analyses, we used customized scripts. The gene expression from Resolve Bioscience was imported in QuPath⁵³. Cells were segmented using StarDist⁵⁴ with the model `dsb2018_heavy_augment.pb` within QuPath and the gene expression was measured by cell. Cells were classified on the basis of their gene expression and counted. Euclidean distances between cell types were measured. To overcome limitations/artefacts based on segmentation, for cell-type and cell-state classification, a number of criteria were set to characterize with high confidence the segmented cells. A customized script included the following parameters for the classification: (1) minimum number of genes; (2) mandatory genes; (3) number of transcripts per gene; and (4) number of genes excluded. To classify the pre-EMT NC stem-like state, a segmented cell was set to express the melanocytic marker *Sox10* and minimum three additional genes, characteristic of this state: *Nes*, *Notch3*, *Celf5*, *Gtse1*, *Dusp15*, *Thra*, *Vcan*, *Espn*. To classify the stress-like (hypoxia) cell state, a segmented cell was set to express *Sox10/Mitf* and a minimum of three additional genes characteristic of this state: *Bnip3*, *Hk2*, *Irx3*, *Pdk1*. To classify ECs, a segmented cell was set to express a minimum of three genes characteristic of this type: *Pecam1*, *Dll4*, *Kdr*, *Cdh5*. To classify pericytes, a segmented cell was set to express *Rgs5* and minimum of two additional genes characteristic for this type: *Acta2*, *Kcnj8*, *Col6a2*. Moreover, to avoid misclassification, cells were set to express low (or be negative) markers from other cell types or cell states. Blood vessels were assigned on the basis of EC presence and the distance of different cell states was calculated based on the nearest distance to each blood vessel (object). The customized scripts are available on request. Furthermore, the gene expression matrix containing cells (>170,000) of all 33 ROIs (without spatial information) was log-normalized and scaled while retaining only cells with at least two features using a customized R script (available on request). Variable features were identified using principal component analysis. Louvain clustering (resolution = 0.3) and subsequent dimension reduction (dims = 1:20) using UMAP were used to project all cells into a two-dimensional UMAP space. To identify malignant melanoma cells, we measured melanocytic gene expression signature (*Pmel*, *Mlana*, *Mitf*, *Sox10*, *Rab27a*, *Car14*, *Tspan10* and *Gsta4*) in all cells using AUCell. Malignant cells were subsetted and reclustered (dims = 1:15, resolution = 0.8) when they showed a melanocytic AUCell value of >0.25 and an absence of endothelial, pericyte and immune markers.

Fluorescence in situ hybridization using RNAscope

Tumour samples were collected and fixed in 4% PFA for 24 h at room temperature. The samples were then dehydrated using an ethanol series followed by xylene and embedded in paraffin using standard procedures. Tissue blocks were cut in 5- μ m-thick sections collected onto Superfrost Plus slides. Multiplex fluorescence in situ hybridization was performed using the RNAscope Multiplex Fluorescent V2 Assay kit (ACDBio, 323100), reagents and probes according to the manufacturer's instructions. RNAscope probes were designed commercially by the manufacturer and are available from Advanced Cell Diagnostics. The following probes were used: *Dll4* (31997), *Sox10* (435931), *Notch3* (425171). The probes were then labelled with TSA opal 520 (PerkinElmer, FP1487001KT), TSA opal 570 (PerkinElmer, FP1488001KT) and TSA opal 690 (PerkinElmer FP1497001KT). The samples were counterstained with DAPI for 5 min and mounted with ProLong Gold Antifade Mountant (Thermo Fisher Scientific, P36930).

Microscope image acquisition

For 2D imaging, slides were acquired on the Zeiss Axio Scan.Z1 ($\times 20$ objective) or on the Vectra Polaris Imaging System. Cryosections with spheres were imaged using the Nikon C2 confocal Microscope. For 3D imaging, image acquisition was performed using the Zeiss LSM 880 Airyscan. All of the images acquired with the Zeiss Axio Scan.Z1 or Zeiss LSM 880 Airyscan were stitched using the Zeiss ZEN 2 software. Images were analysed using Zen 2 (blue edition) or QuPath softwares.

2D quantification of clones with respect to their distance to blood vessels

Sections (thickness, 10 μ m) were quantified by measuring the distance of the clones to the closest blood vessel using QuPath. Vessels were visualized by immunostaining sections for the endothelial markers AQP1 and PECAMI.

Image segmentation and clone reconstruction at the 3D resolution

We quantified cell clusters in 3D sections, which corresponded to z-stacks of (x,y) dimensions between 3.1 \times 3.9 and 5.4 \times 8.4 mm² with a resolution of 0.83 μ m per pixel, and a thickness of 0.45–1.0 mm, with a z-resolution between 5–7 μ m per pixel. The images were processed using a purpose-built segmentation algorithm (implemented in MATLAB R2020a, MathWorks). Every image in the z-stack was transformed to greyscale (MATLAB function `mat2gray`), and its background was subtracted using a moving-average filter with a radius of 500 pixels. We then applied an intensity threshold to the image, retaining only those pixels that belong to the 30th percentile of intensity in that given image (threshold = 0.3). This protocol was applied on both the YFP and RFP channels independently.

With the segmented image, we then proceeded to identify cell clusters. For this, we applied a density-based clustering algorithm (DBSCAN) with a strict 10 μ m distance threshold such that only groups of cells of a common colour tightly packed together would be considered to be part of a given cluster. By measuring the spatial correlation between clusters of the same and different colours, we estimated that clusters separated by a distance of 100 μ m or less (equivalent to about 6–7 cell diameters) were likely to belong to the same clone. By reclustered the data with this threshold, we were able to reconstruct 3D clones, and extract their volumetric information. The clone volumes were then normalized to the typical single-cell volume of about 1,800 μ m³ (or typical diameter of 15 μ m) to construct the clone size distribution as a function of the cell number. The form of the clone size distribution and qualitative features of the data were not affected by variations in the normalization volume. This protocol was applied to both the YFP and RFP channels independently.

After clonal reconstruction, we identified a high fraction of singlets, that is, clones containing a single cell. This fraction was higher than

expected for a proliferative cell population and could either originate from a true subpopulation of non-dividing tumour cells or, alternatively, be fragments of larger clones that could not be assigned to their respective clones due to their large distance of separation. To focus our analysis on the ensemble of clones rooted in tumour cells capable of division, single-cell clones were eliminated from the clonal analysis and statistical modelling, as discussed in the Supplementary Note. The total number of clones and the number of single-cell clones per sample are shown in Supplementary Table 4.

Single-cell suspension of mouse tumours

Tumour samples and metastatic organs isolated from the corresponding mouse melanoma mouse models (allograft or GEMMs) were rinsed in cold Dulbecco's phosphate-buffered saline (DPBS). Tissues were minced into small pieces with sterile scalpels or scissors and incubated 30 min in a heater-shaker at 37 °C 800 rpm in digestion buffer. Tissue samples from each mouse model were enzymatically digested using Liberase (300 µg ml⁻¹, Sigma-Aldrich, 5401127001) and DNase I (1 mg ml⁻¹) diluted in serum free medium (DMEM) and incubated for 30 min at 37 °C. For primary back skin tumours in the *Tyr::cre^{ERT2};Braf^{V600E/+};Pten^{fl}* model, digestion buffer consisted of 0.8 mg ml⁻¹ DNase I (Sigma-Aldrich, 11284932001) and 2 ng ml⁻¹ collagenase P (Sigma-Aldrich, 11249002001) diluted in serum-free medium (DMEM). The digestion mix was inactivated with DMEM containing 10% FBS. To remove excess of red blood cells, when needed, the samples were incubated for 5 min in red blood cell lysis buffer (Thermo Fisher Scientific, A1049201) at room temperature according to the manufacturer's instructions. Single cells were separated from remaining tissue using 40 µm Falcon Cell Strainers (Corning) and resuspended either in FACS buffer (PBS supplied with 2% fetal bovine serum and 2 mM EDTA) or in 0.04% BSA. Cells were then sorted using the BD FACSAria Fusion Flow Cytometer (see below) or counted (either using the Neubauer chamber or the LUNA Automated Cell Counter) to achieve the optimal target cell number (1,000 cells per µl). Cells were processed for 10x scRNA-seq according to the manufacturer's instructions.

Cell sorting

TdTomato cells from the *Prrxl1::cre^{ER}-GFP;Tyr-NRAS^{Q61K/+};Ink4a^{-/-};Rosa26^{LSL-TdTomato/LSL-TdTomato}* model and *Tyr::cre^{ERT2};Braf^{V600E/+};Pten^{fl}* tail model were isolated using a four-laser BD FACSAria Fusion Flow Cytometer (BD Biosciences). Cells were sorted at low pressure (12 psi), using a large 130 µm nozzle to reduce potential cell stress, and cells were kept at 4 °C all of the time. Non-induced mice were used as negative controls for the gating strategy. For the *Prrxl1::cre^{ER}-GFP;Tyr-NRAS^{Q61K/+};Ink4a^{-/-};Rosa26^{LSL-TdTomato/LSL-TdTomato}* model, to exclude a significant fraction of cancer associated fibroblasts (CAFs) that express PRRX1, tumour samples were first incubated with antibodies against the CAF marker α-smooth muscle actin (monoclonal, 1A4), eFluor 660 (ACTA2, 1:500 dilution, Invitrogen, 50-9760-82) for 30 min at 4 °C. Cells were then washed three times with PBS and resuspended in FACS sorting buffer. Cells were incubated with DAPI (dihydrochloride, 1:1,000 dilution, Thermo Fisher Scientific, D3571) for 5 min at room temperature to sort for viable cells. Cell suspensions were kept at 4 °C during the sorting. Cells were sorted based on dead-cell exclusion (DAPI negative), morphological parameters (FSC/SSC), singlet-discrimination, exclusion of the respective markers mentioned above for each model, followed by positive selection of tdTomato-expressing cells. These were collected into 1.5 ml tubes containing FBS. Sorted tdTomato⁺ cells were washed twice with PBS, resuspended in 0.04% BSA and counted using the LUNA Automated Cell Counter to achieve the optimal target cell (1,000 cells per µl). Cell suspensions were then processed for 10x scRNA sequencing. Data were analysed using FlowJo for MAC (v.10.7.1; Becton, Dickinson & Company; 2021).

Single-cell RNA library preparation of mouse tumours

After single-cell suspension preparation, the cells were suspended in 0.04% BSA-PBS, and loaded onto each channel of the Chromium

Single Cell microfluidic chips (V2-chemistry, 10x Genomics) and individually barcoded with a 10x Chromium controller according to the manufacturer's recommendations (10x Genomics). RNA from the barcoded cells was reverse-transcribed, followed by amplification, shearing of the 5' adapter and sample index attachment. The libraries were prepared using the Chromium Single Cell Library Kit v3 (10x Genomics, 1000078) quantified using a low-coverage Illumina NextSeq 550 run and sequenced on the Illumina NovaSeq 6000 instrument.

Single-cell RNA-seq data acquisition and preprocessing

All of the libraries were sequenced on the Illumina NextSeq, HiSeq4000 or NovaSeq6000 until sufficient saturation was reached (73.8% on average). After quality control, the raw sequencing reads were aligned to the mouse reference genome v.mm10-3.0.0, using Cell Ranger (10x Genomics) to obtain feature-barcode matrices.

CNV inference from scRNA-seq data

We inferred copy-number variation (CNV) based on scRNA-seq data by using the R package HoneyBadger (v.0.1)¹⁴. The input for HoneyBadger was the count matrix from the 'RNA' assay of the integrated Seurat object of all cells. The reference for normal cells was the immune cells, which were identified also by AUCell using the immune gene set from ref.¹¹. The mean CNV score was calculated as follows:

$$\text{CNN score} = \frac{\sum_i |G_{\text{CNV},i}|}{n}$$

where *G* is the gene and *i* is the cell.

Single-cell RNA-seq data analysis of *NRAS^{Q61K/+};Ink4a^{-/-}* melanoma samples

Raw count matrices were analysed using the R package Seurat (v.3.1.3)²⁵. The matrices were filtered by removing cell barcodes with <1,000 expressed genes, >7,500 expressed genes and >10% of reads mapping to mitochondrial reads. Next, SCTransformation was applied for normalization. To identify doublets, DoubletFinder (v.2.0.2)⁵⁵ was applied to NRAS_1 (CMA001) and NRAS_3 (CMA079, 080, 081, 082, 083, 084, 085, 086) .rds objects separately assuming that the doublet rate in each sample was 6.1%. Next, all of the Seurat objects were merged, SCTransform was applied regressing out mitochondrial read percentage per cell. Subsequently, data integration was performed using the R package Harmony (v.1.0)⁵⁶. After data normalization and integration, cell cycle scoring was performed, data were filtered for singlets and SCTransform was applied again regressing out the mitochondrial read percentage and cell cycle scores, followed by data integration of this subset as described above. The number of dimensions for Louvain clustering was chosen based on Harmony embedding clustering, driven by a clear variation in embeddings across the cells. To identify malignant cells in the scRNA-seq dataset, three stringent filtration steps were applied. First, the data were subset on the basis of the AUCell score of a malignant gene set acquired from ref.¹⁰, >0.11 or, mean CNV score of >0.13. Subsequently, the cells that passed the first filtration step were filtered based on the superMEL gene set >0.16 or mean CNV score >0.13. Finally, to remove all immune cells, we filtered out cells that were expressing *Ptpnc* (also known as *Cd45*). The malignant subset (16,786 cells) was processed for SCTransform (regressing out mitochondrial read percentage and the cell cycle scores) and harmony integration followed by Seurat (Louvain) clustering (dims = 1:15, resolution = 0.2). Clustering robustness at different resolutions of the Harmony integrated space, as well as the individual tumour samples, was assessed by Silhouette scores⁵⁷.

The marker genes of each Seurat cluster were identified using the FindAllMarkers function in Seurat (Wilcoxon rank-sum test) by comparing each cluster with the remaining ones (Supplementary Table 1).

Article

The top 120–150 overexpressed genes (ranked by adjusted *P* value) per Seurat cluster were analysed by multiple enrichment tools, such as Hyper, Reactome, KEGG, IPA and EnrichR (<https://maayanlab.cloud/Enrichr/>), and a manual literature search (Supplementary Table 2). The top ranked genes per cluster that overlapped with functionally enriched terms were used to establish functional gene signatures (Supplementary Table 3).

Gene regulatory network analysis

SCENIC¹⁷ analysis was run with raw counts from an 'SCT' assay of malignant cells. SCENIC uses gene regulatory network inference, followed by a refinement step using *cis*-regulatory information, to generate a set of refined regulons (that is, transcription factors and their target genes) in the scRNA-seq data. The Python implementation, (pySCENIC: <https://github.com/aertslab/pySCENIC>, v.0.9.19), was run using a Nextflow (v.20.04.1) pipeline (v.0.19.0) (<https://github.com/aertslab/SCENICprotocol>), which streamlined the main steps of the GRN inference and refinement with pySCENIC, as well as the quantification of cellular activity and visualization. The Nextflow pipeline also performed a standard analysis in parallel, using highly variable genes selected on the basis of expression. Differentially activated TF regulons of each malignant cluster were identified using Wilcoxon rank-sum tests against all the cells of the rest of the clusters. We inferred a 'human–mouse conserved' *PRRX1* regulon by intersecting the human *PRRX1* target genes (≥ 10 of 50 occurrences) with the top 120 overexpressed mouse mesenchymal-like genes, which resulted in $n = 38$ overlapping genes.

Mapping of NC development similarities

The activity of different gene expression sets during NC development¹⁸ was quantified in our mouse scRNA-seq dataset using AUCell: neural tube (pre-EMT NC, cluster 12), delaminating, premigratory NC progenitors (cluster 2) and mesenchyme (cluster 3). Binary AUCell score activities were plotted on the UMAP plot (cluster12>0.09(on), cluster2>0.04(on), cluster3>0.05(on)).

Prediction of ligand–receptor interactions

To predict potential ligand–receptor interactions between tumour microenvironment populations and different melanoma cell states, we used the R implementation of NicheNet available at GitHub (<https://github.com/saeyslab/nichenetr>). We focused on the role of ECs (sender) and malignant cluster 4 (receiver) in particular and performed the following dataset and database preprocessing steps: (1) preselection of only overexpressed genes in ECs compared to other tumour microenvironment populations (log-transformed fold change > 0.25); (2) ligand–receptor network generation through https://zenodo.org/record/3260758/files/lr_network.rds, conversion to mouse genes and removal of the 'ppi_prediction_go' and 'ppi_prediction' databases while ligands had to be expressed among sender and receptors among receiver cells; (3) signalling network generation by downloading https://zenodo.org/record/3260758/files/signaling_network.rds, conversion to mouse genes, while all genes had to be expressed in receiver cells; (4) gene regulatory network generation by importing the results of the SCENIC analysis while all genes had to be expressed in receiver cells; (5) to generate weighted networks, we used as the input ligand–receptor, signalling and gene regulatory networks. The weight of every protein interaction pair is proportional to the number of hits among different databases and is then more likely to be a true interaction pair; (6) to generate the ligand–target matrix, we used the weighted networks and ligands as input. This matrix was used for the NicheNet analysis pipeline. To validate the DLL4–NOTCH3 interaction predicted by NicheNet, we ran another cell–cell interaction algorithm, CellChat²⁹. To do so, we used the Seurat object and ran CellChat (v.1.1.3) applying a 10% truncated mean for the average gene expression per cell group and a minimum of 20 cells required per cell group for cell–cell communication.

Patient biopsy collection and scRNA-seq data analysis

Baseline tumour biopsies from 22 patients (23 samples, of which 20 had malignant cells detected in the single-cell pool) with locally advanced or metastatic melanoma (stage IIIB–IV) from lymph nodes ($n = 14$), skin ($n = 5$) and subcutis ($n = 4$). Most patients ($n = 14$) were treatment naive when the samples were collected. Written informed consent was obtained from all of the patients. Biopsies were collected from different metastatic sites. Two patients had received previous systemic treatment in the adjuvant setting. One patient had previously received three cycles of neo-adjuvant chemotherapy for a metachronous non-small cell lung carcinoma (SPECIAL; UZ Leuven; s62275). This study was approved by UZ Leuven Medical Ethical Committee.

Methods for tumour dissociation, library construction and sequencing, scRNA-seq data acquisition and analysis were described previously²². Data from ref. ¹¹ (cell annotation and count matrix) were acquired from the Gene Expression Omnibus (GEO: GSE115978) and the signatures were measured as described above. For both datasets, we measured the activity of each functional NRAS model-derived state in all individual human cells using the functional signatures (Supplementary Table 3). Next, these signature genes were used to generate scores using AUCell¹⁷. A binary cut-off (ON/OFF) was applied based on AUCell score distributions. We discarded all cells in which more than one transcriptional program was evaluated as ON to retain only cells that could be assigned to a specific state with high confidence.

Single-cell RNA-seq data analysis of *Braf*^{V600E/+};*Pten*^{+/l} tumour samples

Single-cell RNA-seq data from *Braf*^{V600E/+};*Pten*^{+/l} tail and back skin tumour samples ($n = 2$) were analysed as described above. Cells with more than 500 and less than 6,000 genes and less than 10% mitochondrial genes expressed were filtered out for further analyses. The *Braf*/*Pten* model is considered to have lower CNV aberrations and, indeed, we observed that the mean CNV score was not sufficient to separate normal cells from tumour cells. We therefore selected malignant cells on the basis of a high AUCell SuperMEL score or positivity of tdTomato expression. The SuperMel signature was derived from the differential gene expression analysis of malignant versus CAF clusters. It represents the top 14 genes upregulated (*Copg2*, *Cd59a*, *Nceh1*, *Cdh19*, *Gjc3*, *Cers4*, *Sort1*, *Plekhb1*, *Pax3*, *Sox10*, *Rapgef4*, *Kcnn4*, *Akr1b7*, *Syng1*) in malignant clusters (adjusted $P < 1.0 \times 10^{-300}$) with at least 90% of malignant cells expressing these markers compared with less than 35% for CAFs. Next, we clustered the cells using the same method as described for the NRAS model. Marker genes per cluster were called using the standard Seurat pipeline, and AUCell scores of the functionally enriched top 100 marker genes (Supplementary Table 1) from melanocytic, neural crest-like, pre-EMT NC stem-like and mesenchymal-like NRAS model states were measured across all cells.

Single-cell RNA-seq data analysis from the *Prrx1::cre*^{ER-GFP};*Tyr-NRAS*^{Q61K/c};*Ink4a*^{-/-};*Rosa26R*^{LSL-tdTomato/LSL-tdTomato} model

TdTomato⁺-sorted (primary and lung, early and late) cells were analysed as described above. Cells with more than 500 and less than 7,500 genes and less than 10% mitochondrial genes expressed were used for further analyses. After correcting for multiplets using DoubletFinder (7.6% doublet rate), singlets were processed using SCTransform (regressing out the mitochondrial read percentage and the cell cycle scores) and harmony integration followed by Seurat (Louvain) clustering.

Early-labelled primary tumour cells (*Mitf*low expressing cells, negative for *Krt14*, *Pecam1* and *Lum*) were subclustered and examined for mesenchymal, melanoma lineage marker expression and pre-EMT NC stem-like signature activities. Early- and late-labelled lung metastatic melanoma cells (*Mitf* and *Mlana* enriched Seurat cluster 6 resolution = 0.4, dims = 1:15) were subclustered and examined for pigmentation marker expression.

Single-cell RNA-seq data analysis of *NRAS*^{Q61K}/*Ink4a*^{-/-} and bEnd.3 cell co-culture

scRNA-seq data from the *NRAS*^{Q61K}/*Ink4a*^{-/-} cell line (expressing watermelon construct) as the control and *NRAS*^{Q61K}/*Ink4a*^{-/-} cells co-cultured with bEnd.3 cell line were analysed as described above. Cells with more than 2,000 and less than 7,000 genes and less than 7% of mitochondrial genes expressed were filtered out for further analyses. Moreover, for direct comparison of only malignant cells between the test and control samples, ECs (positive for *Pecam1* expression) were also removed. Single-cell data were processed as described above. However, in this analysis, we did not perform harmony integration, as we measured only AUCell scores of the top 100 marker genes for melanocytic, neural crest-like, pre-EMT NC and mesenchymal-like *NRAS* model states. Differential gene expression between the two samples was performed using the standard Seurat pipeline.

Bulk RNA-seq after genetic inactivation of *PRRX1* in human melanoma cells

Total RNA was extracted using the NucleoSpin RNA kit (Macherey Nagel, 740955). The RNA integrity was monitored using Bioanalyzer analysis (Agilent; RNA integrity number: 9.7–10). About 500 pg of RNA per sample was reverse-transcribed and amplified using a modified SMARTseq2 protocol⁴. Before generating sequencing libraries using the NexteraXT kit (Illumina, FC-131-10), cDNA profiles were monitored using the Bioanalyzer. Sequencing was performed on the NextSeq500 platform (Illumina, single-end 75 bp reads). Differential analyses between siPRRX1 and siControl samples were performed using the DeSeq2 pipeline.

Human melanoma cell lines

The human melanoma cultures were derived from patient biopsies by the Laboratory of Oncology and Experimental Surgery (G. Ghanem, Institute Jules Bordet). All of the cell lines were grown in 5% CO₂ at 37 °C in F10 supplemented with 10% FBS, 0.25% GlutaMAX and penicillin–streptomycin antibiotics. Cells were tested for mycoplasma contamination.

Generation of a watermelon-positive *NRAS*^{Q61K}/*Ink4a*^{-/-} cell line

The watermelon library⁵⁸ and backbone are available at Addgene (155257 and 155258). An established mouse *NRAS*^{Q61K}/*Ink4a*^{-/-} cell line was transduced using the watermelon virus in DMEM medium supplemented with 10% FBS in presence of 16 µg ml⁻¹ polybrene (Sigma-Aldrich). After incubation for 24 h with virus, the medium was changed for medium without polybrene. Then, 48 h after infection, the cells were sorted for mNeon expression and expanded in culture for 3–5 passages before being aliquoted to 10 × 10⁶ cells per vial and stored at –80 °C. The cells were tested for mycoplasma contamination.

Lentiviral production

HEK293 FT cells were transfected with dVPR and VSVG packaging plasmids using Lipofectamine 2000 reagent (Thermo Fisher Scientific) according to the manufacturer's instructions. Then, 24 h after transfection, the medium was replaced with DMEM medium (Thermo Fisher Scientific) supplemented with 20% FBS. Medium containing virus particles was collected 48 h after transfection. Virus particles were filtered through a 0.45 µm syringe filter and concentrated using the Vivaspin 20, 50,000 MWCO 20 ml columns (Sigma-Aldrich) in a cold centrifuge at 3,000g to a final volume of 2 ml (30–60 min). Virus was aliquoted and stored at –80 °C until use. Virus titre was estimated by measuring fluorescence using flow cytometry.

mCherry dilution FACS experiments

Watermelon cells were thawed and expanded in DMEM medium supplemented with 10% FBS for 2–3 days before induction with doxycycline (dox) at a concentration of 2 µg ml⁻¹ (pulse). After a 48 h pulse,

mCherry expression were monitored using the IncuCyte (Sartorius) live-imaging system. The cells were then seeded into 10 cm plates either alone or together with bEnd.3 cell lines at a ratio of melanoma cells to endothelial cells of 1:2 in DMEM medium supplemented with 10% FBS, 1% sodium pyruvate and 1% HEPES. Then, 48 h later (chase), cells were trypsinized for 3 min to detach the melanoma cells but not the endothelial cells and then resuspended in FACS buffer (2% FBS, 1 mM EDTA, 25 mM, HEPES pH 7.0 in phosphate-buffered saline). Cells were then filtered through a 40 µm strainer. mCherry expression in watermelon cells (mNeon-positive cells) was measured by FACS (SONY MA9000 or BD Fortessa X-20) and analysed in FlowJo.

3D monoculture and co-culture

The *NRAS*^{Q61K}/*Ink4a*^{-/-} cell line stably expressing dsRed and the bEnd.3 cell line stably expressing GFP were seeded at a total number of 3,000 cells per well into 96-well ultra-low attachment plates (Thermo Fisher Scientific Nunclon) at a different ratio in DMEM medium supplemented with 10% FBS, 1% sodium pyruvate and 1% HEPES. The growth of cells was monitored using the IncuCyte Zoom (Sartorius) live-imaging system for 10 days. For quantification, the size of spheres was measured using the Zoom software. Three measurements were taken for each sphere and the average of three values was used to calculate the volume.

3D culture staining

3D spheres were collected and pooled together in 1.5 ml Eppendorf tubes. Spheres were then transferred into disposable base moulds 7 × 7 × 5 mm to be embedded in Tissue-Tek OCT Compound (Sakura Finetek, 4583) and stored at –80 °C. Sections of 10 µm were cut using the Thermo Fisher Scientific CryoStar NX70 Cryostat. The sections were stored in the short term at –20 °C. Staining was performed according to the protocol described above for mouse frozen section immunofluorescence.

siRNA-mediated transient genetic inactivation

Cells were transfected with the indicated specific siRNA molecules using the Lipofectamine 2000 Transfection Reagent (Invitrogen) according to manufacturer's protocol. siRNAs were used at a final concentration of 100 nM for *PRRX1* and 80 nM for *Notch3* (Dharmacon, L-047867-01-0005).

For bulk RNA-seq of MM047 after treatment with siPRRX1, 2 × 10⁵ cells were plated 1 day before transfection in a six-well plate. Cells were collected 48 h after transfection. RNA was extracted using the RNA NucleoSpin extraction kit (Macherey & Nagel) according to the manufacturer's instructions. *PRRX1* silencing was achieved by pooling at a 1:1 ratio of siRNAs targeting the *PRRX1A* and *PRRX1B* isoforms purchased from Dharmacon. For *PRRX1A* the siRNAs were: 5'-AAGAUGUUGUUUACACGAGGG-3' (HA09071733) and 5'-CCCUCGUGUAAACAACAUUU-3' (HA09071734). For *PRRX1B* the siRNAs were: 5'-GACAGCGUCUCCGUACAGCGC-3' (HA09071735) and 5'-GCGCUGUACGAGACGUGUC-3' (HA09071736). For *Notch3*, a pool of 4 siRNAs at a final concentration of 80 nM was used: (1) 5'-CCACGUGUCUUGACCGAAU-3', (2) 5'-GAACGUGUGUACGGUGU-3', (3) 5'-GCACUUUGUGAGCGAAA-3' and (4) 5'-GGAUAGGCUUUCGUGCA-3'. Control samples were transfected with non-targeting siRNA pool (Dharmacon, D-001810-10-20).

Matrigel invasion assay and quantification

The invasive activity of melanoma cells was determined by Matrigel Transwell invasion assays using Boyden chambers (0.8 mm BD Bio-Coat Matrigel Invasion Chambers; Corning, 354480), according to the manufacturer's guidelines. In brief, MM099 cells were starved overnight with FBS and L-glutamine-deprived medium. Next, 2 × 10⁵ cells were plated in each invasion chamber in FBS-deprived medium, while FBS (10%) and L-glutamine-enriched medium (2.5%) was used in the wells placed in the lower chamber. Uncoated inserts were used as a control

Article

for proliferation. Then, 72 h after seeding, the membranes were stained with crystal violet and subsequently imaged.

Cells were quantified using the ImageJ plugin Colony Area to quantify the intensity-weighted area percentage (the intensity of staining for each pixel)⁵⁹. Each sample was then normalized to the control well and statistical significance was assessed using unpaired two-tailed *t*-tests.

RT-qPCR

Cells were resuspended in QIAzol using the miRNeasy Kit and processed according to the manufacturer's instructions (QIAGEN) or in RA1 lysis buffer using the RNA NucleoSpin extraction kit (Macherey&Nagel). RNA was quantified using the NanoDrop 1000 (Thermo Fisher Scientific) system and 500–2,000 ng RNA was reverse transcribed using the High-Capacity cDNA Reverse Transcription Kit (Life Technologies). qPCR reactions were performed using the Fast SYBR Green Master Mix (Life Technologies) and run on a Roche LightCycler-480-384. Data processing with qbase+ v.2.6 software (Biogazelle) relies on normalization to a minimum of two reference genes. qPCR with reverse transcription (RT-qPCR) primer sequences were as follows: for *PRRX1*, forward 5'-CAGGACAATGACCAGCTGAACTC-3' and reverse 5'-TGTGTCGCTCAAAGACACG-3'; for *ACTB*, forward 5'-CTGGAACGGTGAAGGTGACA-3' and reverse 5'-AAGGGACTTCCTGTAAC\AATTCATG-3'; for *RPL13A*, forward 5'-CCTGGAGGAGAAGAGAAAGAGA-3' and reverse 5'-TTGAGGACCTCTGTATTGTCAA-3'; and for *SDHA*, 5'-TGGGAACAAGAGGGCATCTG-3' and reverse 5'-CCACCACTGCATCA

Data analysis

Pooled data are presented as mean \pm s.e.m. unless otherwise indicated. Information regarding sample size, error bars and statistical analysis used is described in each figure legend. *P* values for statistical analysis of two experimental groups or for multiple comparisons were calculated using Microsoft Excel 2016 and GraphPad Prism (v.9.2.0) (<https://www.graphpad.com>).

Reporting summary

Further information on research design is available in the Nature Research Reporting Summary linked to this article.

Data availability

Raw data of scRNA-seq (and output files from CellRanger) and spatial transcriptomics (Visium and stereo-seq) are deposited at the GEO under accession number GSE207592. Processed count matrices and cell annotations (scRNA-seq and Visium) are available online (<https://marine-lab.sites.vib.be/en>). Molecular cartography data are available at Zenodo (https://zenodo.org/record/6856193#_ytj-fnZBz-g). All other data supporting the findings of this study are available on reasonable request. Source data are provided with this paper.

Code availability

Scripts and annotation files for the study have been deposited at GitHub (<https://github.com/MarineLab/Karras-et-al>). The raw list of clone sizes and scripts to extract the model parameters, as well as running the stochastic simulations of the two-compartment model, are available at GitHub (https://github.com/ibordeu/scripts_Karras_et_al_2022_git). A brief description of how to reproduce the analysis workflows and the figures presented in this paper is included there.

43. Bosenberg, M. et al. Characterization of melanocyte-specific inducible Cre recombinase transgenic mice. *Genesis* **44**, 262–267 (2006).
44. Krimpenfort, P., Quon, K. C., Mooi, W. J., Loonstra, A. & Berns, A. Loss of p16^{INK4a} confers susceptibility to metastatic melanoma in mice. *Nature* **413**, 83–86 (2001).
45. Dankort, D. et al. *Braf*^{V600E} cooperates with *Pten* loss to induce metastatic melanoma. *Nat. Genet.* **41**, 544–552 (2009).

46. Maria Bosisio, F. et al. Functional heterogeneity of lymphocytic patterns in primary melanoma dissected through single-cell multiplexing. *eLife* <https://doi.org/10.7554/eLife.53008> (2020).
47. Susaki, E. A. et al. Whole-brain imaging with single-cell resolution using chemical cocktails and computational analysis. *Cell* **157**, 726–739 (2014).
48. Frankish, A. et al. GENCODE reference annotation for the human and mouse genomes. *Nucleic Acids Res.* **47**, D766–D773 (2019).
49. Yates, A. D. et al. Ensembl 2020. *Nucleic Acids Res.* **48**, D682–D688 (2020).
50. Marçais, G. & Kingsford, C. A fast, lock-free approach for efficient parallel counting of occurrences of *k*-mers. *Bioinformatics* **27**, 764–770 (2011).
51. Gans, J. D. & Wolinsky, M. Improved assay-dependent searching of nucleic acid sequence databases. *Nucleic Acids Res.* **36**, e74 (2008).
52. Rodriguez, J. M. et al. APPRIS 2017: principal isoforms for multiple gene sets. *Nucleic Acids Res.* **46**, D213–D217 (2018).
53. Bankhead, P. et al. QuPath: open source software for digital pathology image analysis. *Sci. Rep.* **7**, 16878 (2017).
54. Schmidt, U., Weigert, M., Broaddus, C. & Myers, G. Cell detection with star-convex polygons. In *Proc. Medical Image Computing and Computer Assisted Intervention—MICCAI 2018* (eds Frangi, A. et al.) Vol. 11071, 265–273 (Springer, 2018).
55. McGinnis, C. S., Murrow, L. M. & Gartner, Z. J. DoubletFinder: doublet detection in single-cell RNA sequencing data using artificial nearest neighbors. *Cell Syst.* **8**, 329–337 (2019).
56. Korsunsky, I. et al. Fast, sensitive and accurate integration of single-cell data with Harmony. *Nat. Methods* **16**, 1289–1296 (2019).
57. Rousseeuw, P. J. Silhouettes: a graphical aid to the interpretation and validation of cluster analysis. *J. Comput. Appl. Math.* **20**, 53–65 (1987).
58. Oren, Y. et al. Cycling cancer persister cells arise from lineages with distinct programs. *Nature* **596**, 576–582 (2021).
59. Guzmán, C., Bagga, M., Kaur, A., Westermarck, J. & Abankwa, D. ColonyArea: an ImageJ plugin to automatically quantify colony formation in clonogenic assays. *PLoS ONE* **9**, e92444 (2014).

Acknowledgements We thank G. Ghanem for providing us with the MM lines; H. Clevers for providing us with the Confetti-reporter mouse strain; and O. Van Goethem and V. Benne for their assistance with the mouse experiments; the members of the VIB Technology Watch members, M. Bontinck and Y.-C. Wang, for facilitating collaborations with Resolve Biosciences and BGI research, respectively; and Y. Oren and the laboratories of A. Regev and J. Brugge for providing the watermelon vector. P.K. received financial support from an Marie Curie Individual Fellowship (H2020-MSCA-IF-2018, 841092), FWO (1210520N) and Stichting tegen Kanker (Foundation against Cancer, 2021-028). J.P. received financial support from a Marie Curie Individual Fellowship (H2020-MSCA-IF-2019, 896897). A.N. received postdoctoral from the KU Leuven (PDMT1/21/035). C.P. received PhD research fellowships from FWO (11M3822N) and of the Boehringer Ingelheim Fonds. J.W. received a postdoctoral research fellowship from Stichting Tegen Kanker (Foundation against Cancer; 2019-100). O.M.-B. was supported by the 12T1217N project by the FWO at the program under the Marie Skłodowska-Curie grant agreement no. 665501. D.P. and N.V.D. received PhD fellowships from the VIB PhD international programme and FWO-SB 1S79619N, respectively. F.R. acknowledges support from the Alexander von Humboldt Foundation. The computational resources and services used in this work were provided by the VSC (Flemish Supercomputer Centre), funded by the Research Foundation—Flanders (FWO) and the Flemish Government, department EWI. B.D.S. acknowledges funding from the Royal Society E. P. Abraham Research Professorship (RP\R1\180165), EPSRC (EP/P034616/1) and Wellcome Trust (219478/Z/19/Z). This work was supported by the FWO (G0C530N and G070622N), Stichting Tegen Kanker (FAF-F/2018/1265), Neftkens foundation, Melanoma Research Alliance (MRA, EIA#623591), KU Leuven (C1 grant) and the Belgian Excellence of Science (EOS) programme to J.-C.M.

Author contributions P.K. designed and conducted experiments, and acquired, analysed and interpreted the data. P.K., I.B. and B.D.S. acquired, analysed and interpreted data for the mathematical modelling. P.K. generated the mouse models and performed all the in vivo experiments assisted by C.P.; P.K. performed all of the single-cell mouse experiments on the NRAS background, and G. Bervoets and E.L. performed all of the single-cell human biopsies. N.V.R. and E.L. performed the single-cell experiments in the BRAF background. F.R., J.P. and Y.H. analysed the single-cell data from mouse and human lesions and data from TCGA. A.N. conducted in vitro experiments of melanoma–endothelial cell interplay. M.D., D.P. and J.W. conducted and analysed in vitro experiments to assess PRRX1 function in melanoma. P.K. and S.M. conducted spatial transcriptomics experiments, and analyses were performed by F.R. and R.B.; P.K., F.R., J.H.K., H.L. and X.Z. performed the stereo-seq experiments and downstream analyses. O.M.-B. and J.L. provided support for the FACS sorting/analysis. B.P. provided computational support for molecular cartography experiments. O.B., Y.V.H., F.B. and J.v.d.O. provided human samples and pathology support. A.R. provided the *Prrx1::cre^{ER}-IRES2-EGFP* allele mice. G. Bergers, Y.S., D.L. and C.B. helped with the interpretation of all data and concepts underlying the perivascular niche and mode of tumour growth. All of the authors read and edited the manuscript. P.K., F.R. and J.-C.M. conceptualized and designed the research study and wrote the manuscript.

Competing interests The authors declare no competing interests.

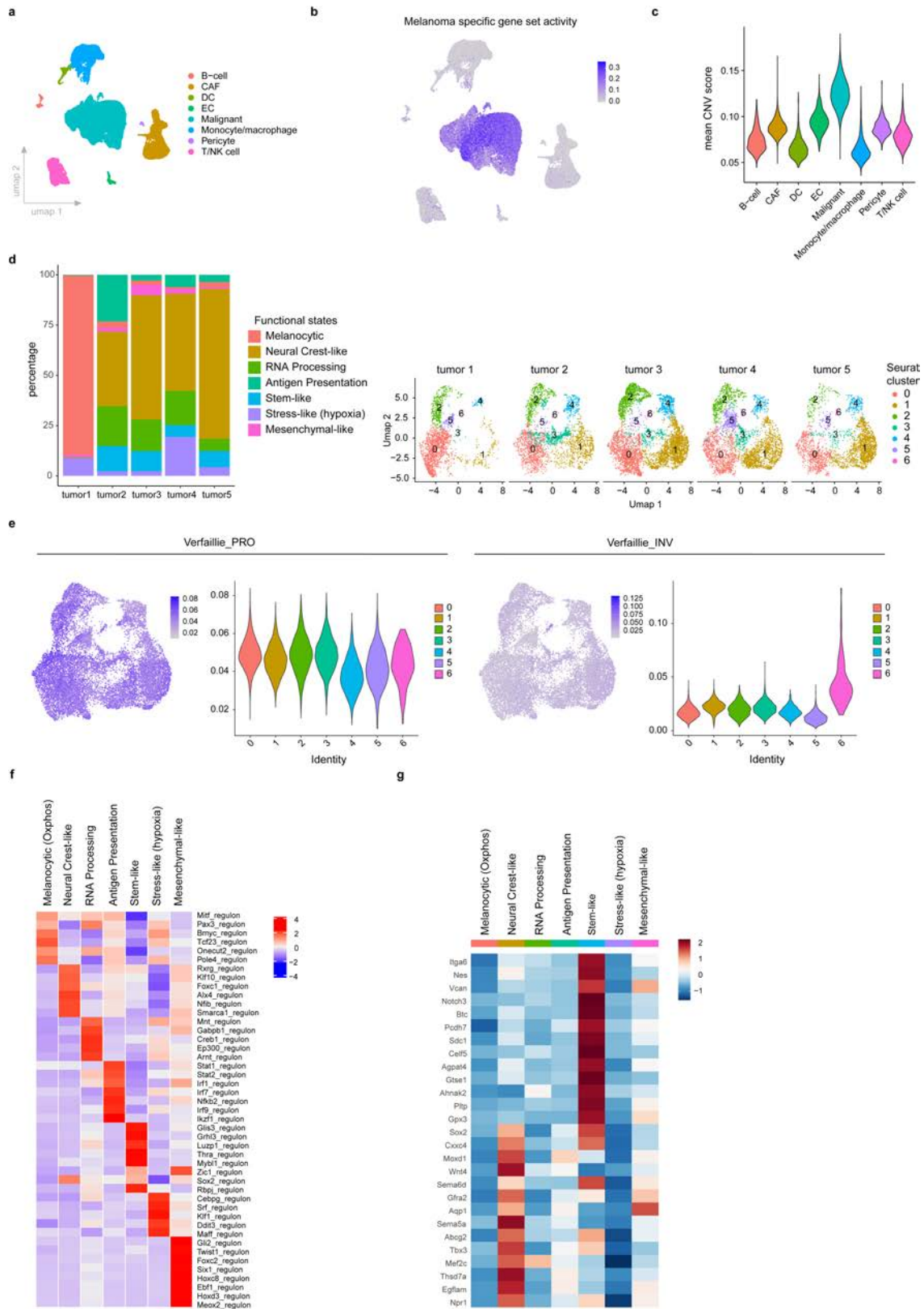
Additional information

Supplementary information The online version contains supplementary material available at <https://doi.org/10.1038/s41586-022-05242-7>.

Correspondence and requests for materials should be addressed to Florian Rambow or Jean-Christophe Marine.

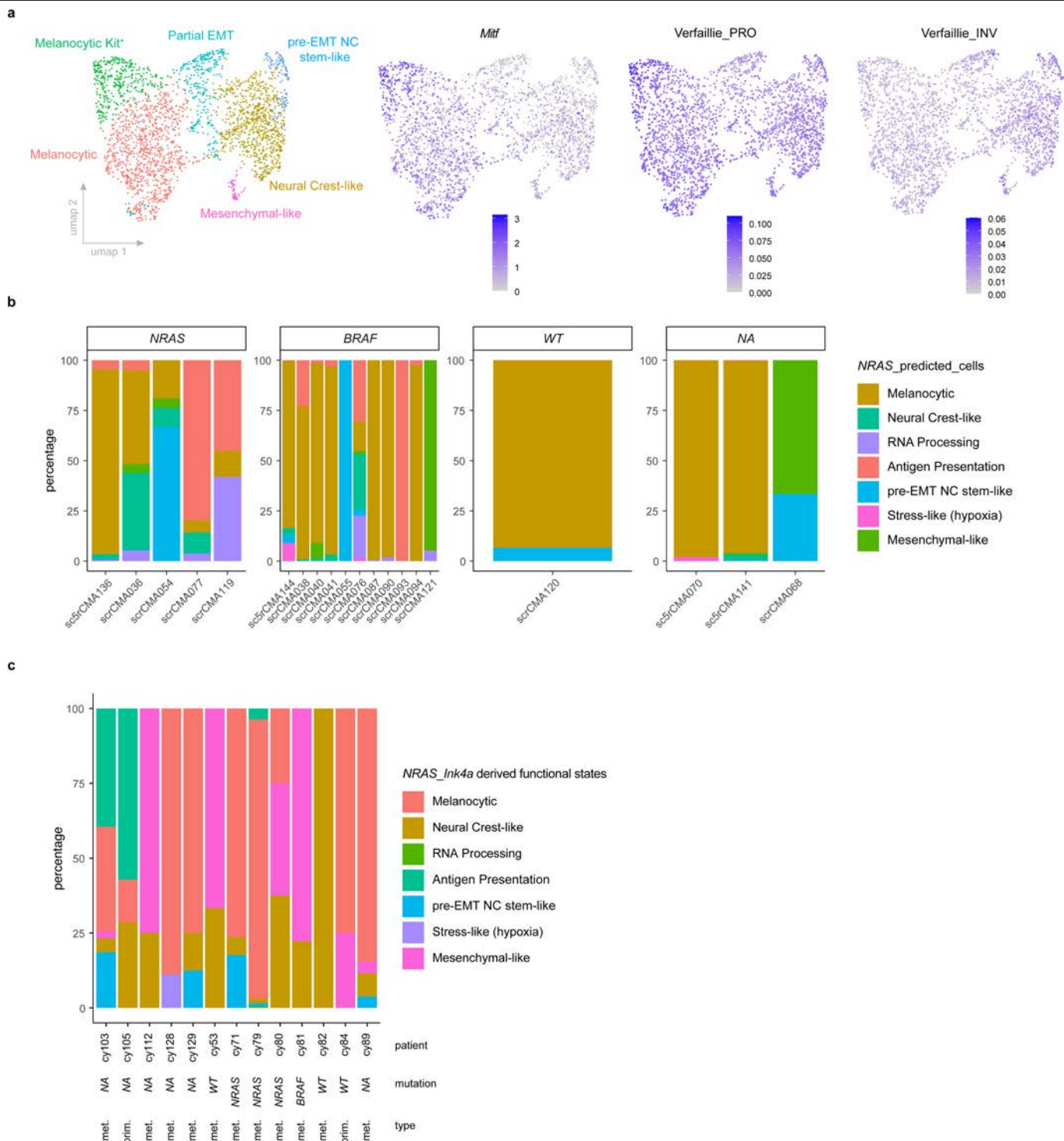
Peer review information Nature thanks Thomas Hofer, Samantha Morris, Frederic de Sauvage and Amaya Viros for their contribution to the peer review of this work.

Reprints and permissions information is available at <http://www.nature.com/reprints>.



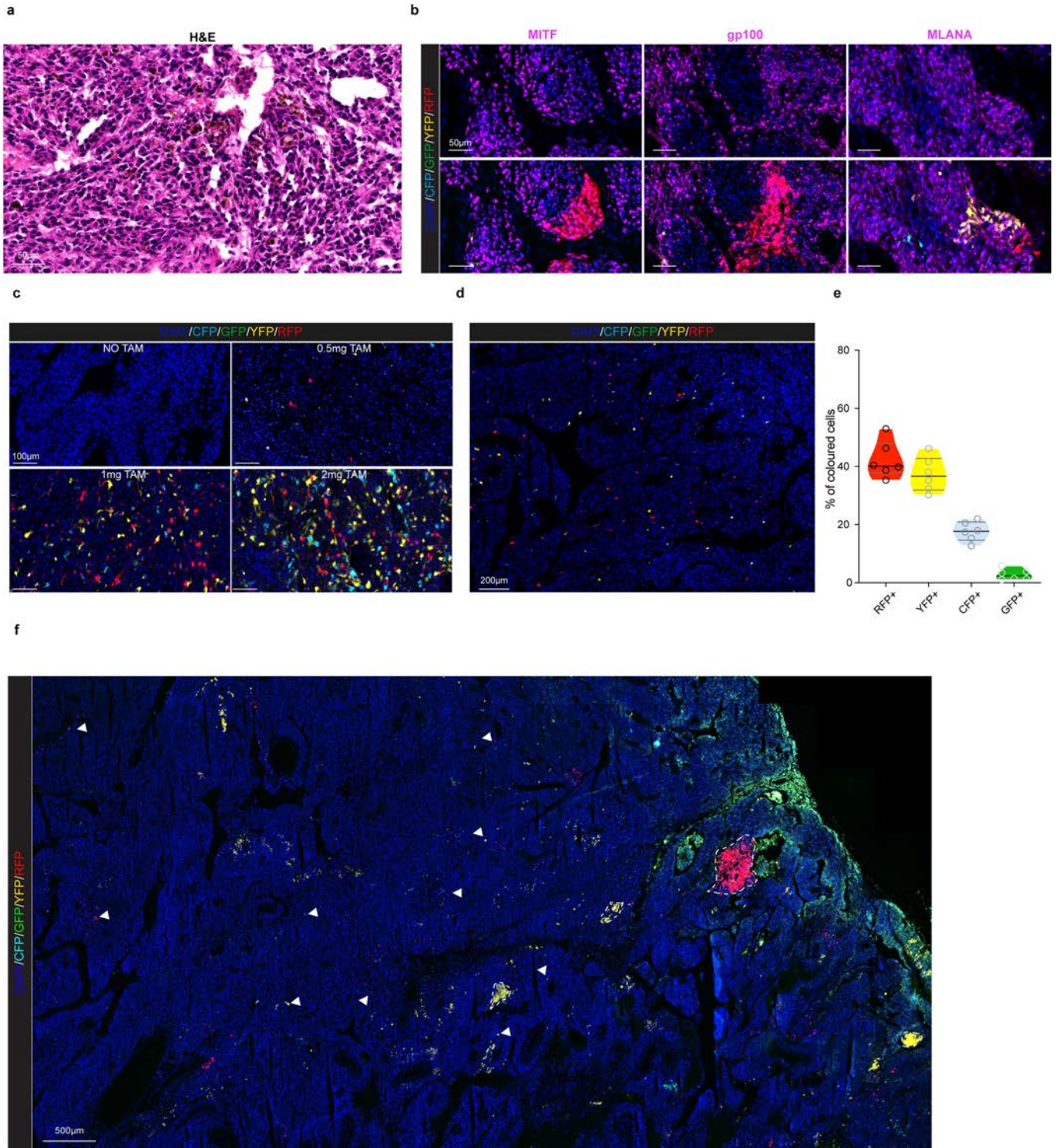
Extended Data Fig. 1 | Cellular composition and discriminative regulons of *NRAS*-driven mouse melanoma. **a**, UMAP illustrating cell type diversity in *NRAS*^{Q61K/+};*Ink4a*^{-/-} lesions (43k cells). **b**, Activity (AUCell score) of a melanoma specific gene set⁵ in *NRAS*^{Q61K/+};*Ink4a*^{-/-} lesions. **c**, Violin plot depicting mean Copy Number Variation (CNV) scores for the different cell types, including the malignant compartment, identified in *NRAS*^{Q61K/+};*Ink4a*^{-/-} lesions. **d**, Relative proportions of the melanoma transcriptional cell states highlighting a strong representation across all 5 *NRAS*^{Q61K/+};*Ink4a*^{-/-} tumours, illustrated as stacked

bar (left panel) and as UMAP (right panel). **e**, Proliferative (PRO or melanocytic) and invasive (INV or mesenchymal-like) gene sets³⁴ activity (AUCell score) in all mouse malignant cells (umap plots, left panel) or per transcriptional state (violin plots, right panel). **f**, Heatmap depicts changes in regulon activities for seurat clusters described in *NRAS*^{Q61K/+};*Ink4a*^{-/-} lesions. **g**, Heatmap depicting average expression of selected Neural Crest Stem Cell (NCSC) and pre-migratory (pre-EMT) Neural Crest markers.



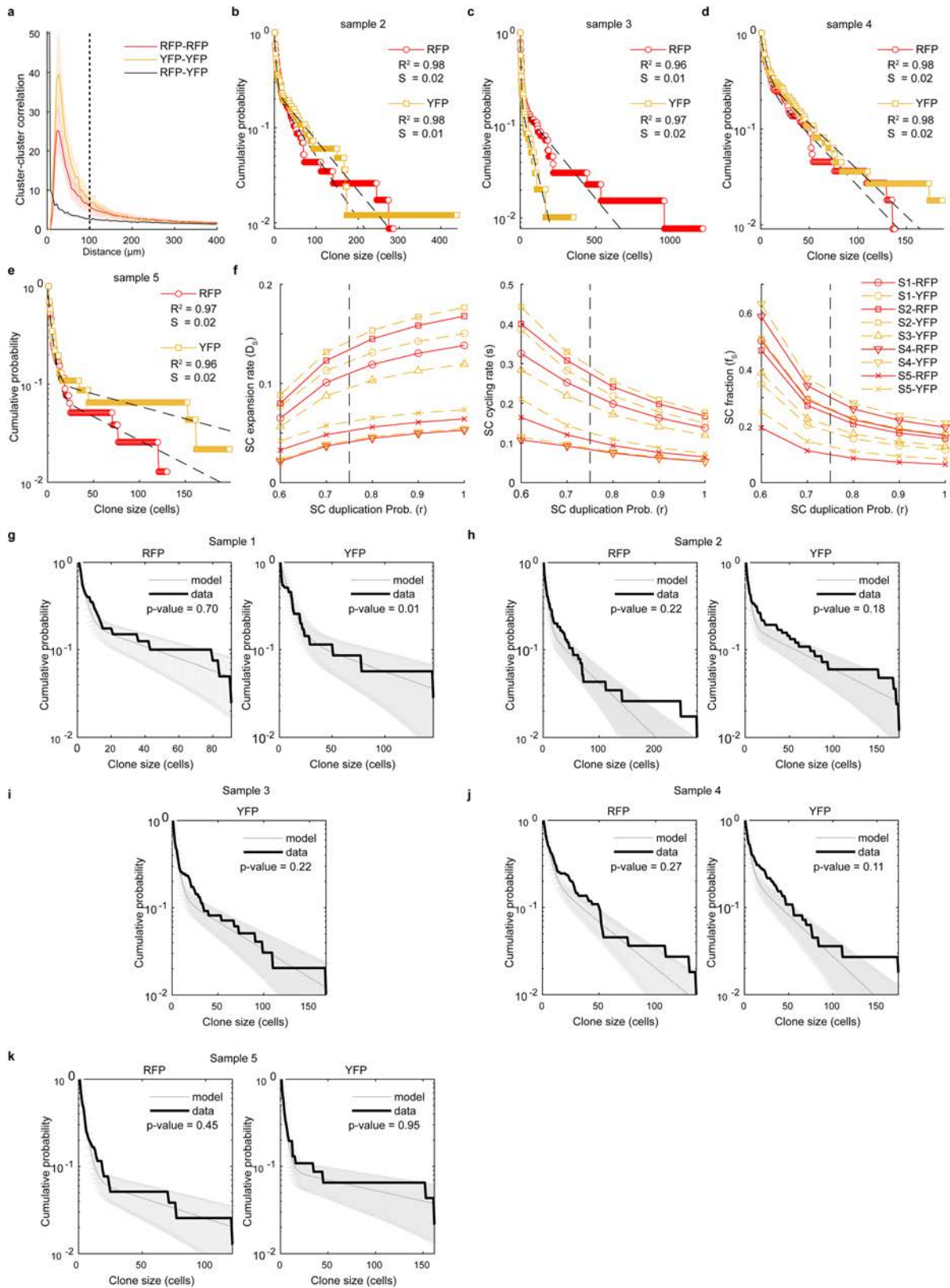
Extended Data Fig. 2 | Single-cell transcriptomic landscape in BRAF-mutant mouse and human melanoma lesions. a, UMAP visualization of >2.600 malignant cells analysed by scRNA-seq and integrated across 2 different *BRAF*^{V600E};*Pten*^{fl} lesions. The Seurat clusters were annotated using signature-based annotation (left panel). *Mitf* expression and Proliferative (PRO or Melanocytic) and invasive (INV or mesenchymal-like) gene sets³⁵ activity (AUCell score) across all malignant cells (right panels). **b**, Stacked bar chart illustrating the distribution of malignant cell states (binary cut-offs) extracted from *NRAS*^{Q61K};*Ink4a*^{-/-} and projected onto scRNA-seq data of drug naïve human melanoma lesions. Each graph is categorized based on the main

genetic driver mutations identified. WT indicates lesions that do not carry BRAF neither NRAS mutations; N/A indicates lesions for which genetic information is lacking. **c**, Stacked bar chart illustrating the distribution of malignant cell states (binary cut-offs) extracted from *NRAS*^{Q61K};*Ink4a*^{-/-} lesions and projected onto a publicly available scRNA-seq dataset (malignant treatment-naïve cells) of human melanoma biopsies¹¹. The patient IDs and main genetic driver mutations are indicated. WT indicates lesions that do not carry BRAF neither NRAS mutations; N/A indicates lesions for which genetic information is lacking; met. stands for metastatic and prim. for primary lesions.



Extended Data Fig. 3 | Characterization of the Confetti melanoma mouse model. **a**, H&E staining of melanoma model *Tyr::NRAS^{Q61K/+}; Ink4a^{-/-}; Tyr::CreER^{T2/+}; Rosa26^{LSL-Confetti^{+/+}}*. Representative image from n = 3 independent tumours. **b**, Confocal images of labelled melanoma subclones acquired by confocal imaging upon TAM administration and immunostained for melanocytic lineage markers MITF, gp100 and MLANA (magenta) exhibiting heterogeneous expression. Images from n = 4 independent tumours. **c**, Representative confocal images showing Confetti labelling efficiency in melanoma tumours 3 days after the administration of different doses of TAM in order to achieve the optimal dose to perform clonal analyses. Images from n = 4 independent experiments. **d**, Representative confocal images showing Confetti labelling of

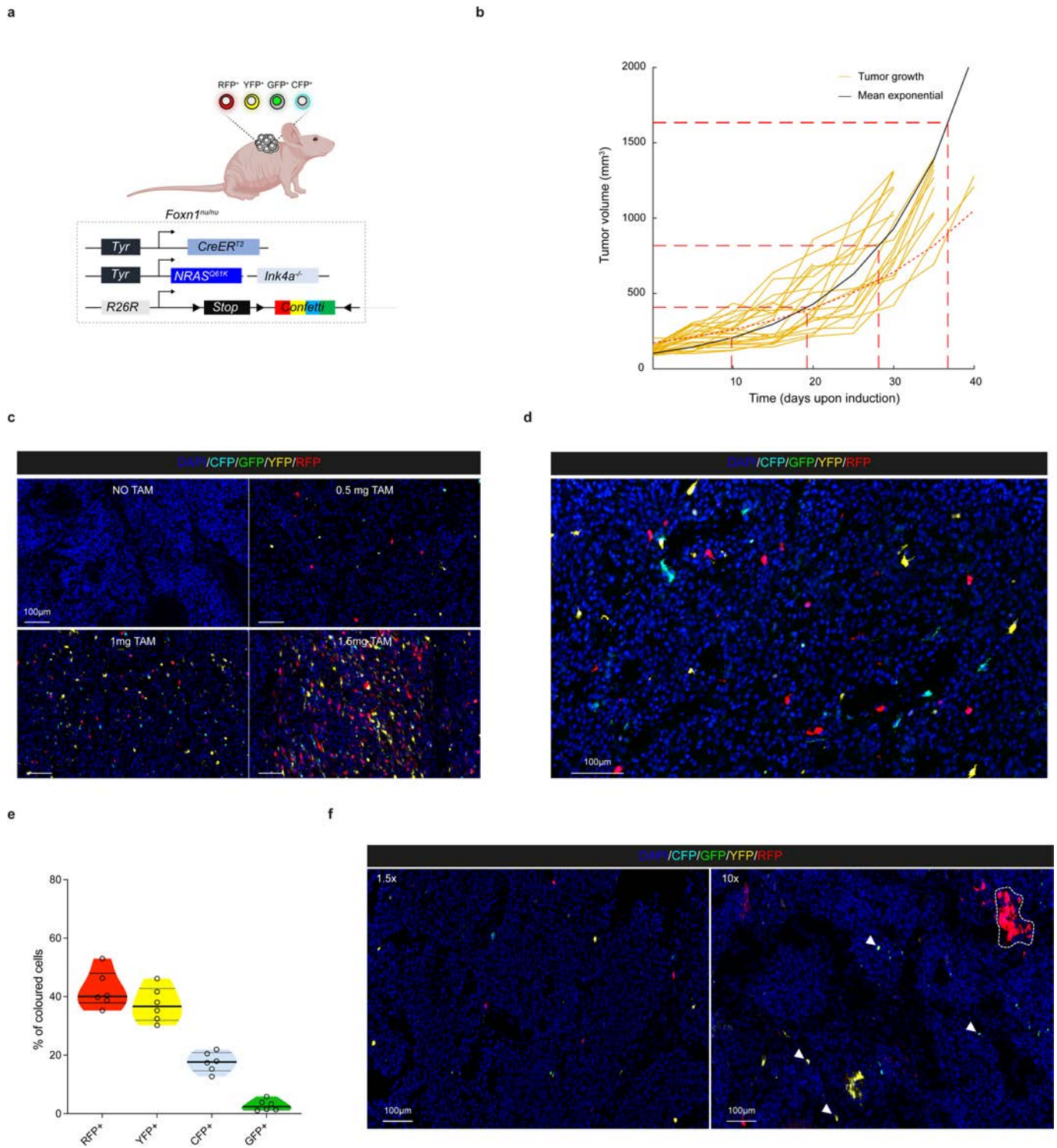
melanoma cells 5 days after TAM administration (0.5 mg). Images from n = 6 independent tumours. **e**, Violin plot depicting the proportion of labelled melanoma cells expressing each Confetti fluorophore 5 days after TAM administration (0.5 mg). Six melanoma tumours (two sectional areas of each) were analysed. Black line represents median and grey lines the 25th to 75th percentile. **f**, Representative confocal image at low magnification illustrating the clone size heterogeneity in tumours that have expanded 10-fold from the initial size after TAM administration (0.5 mg). Arrowheads show several single and/or oligoclones that exhibit minor expansion over time. Images from n = 8 independent tumours.



Extended Data Fig. 4 | See next page for caption.

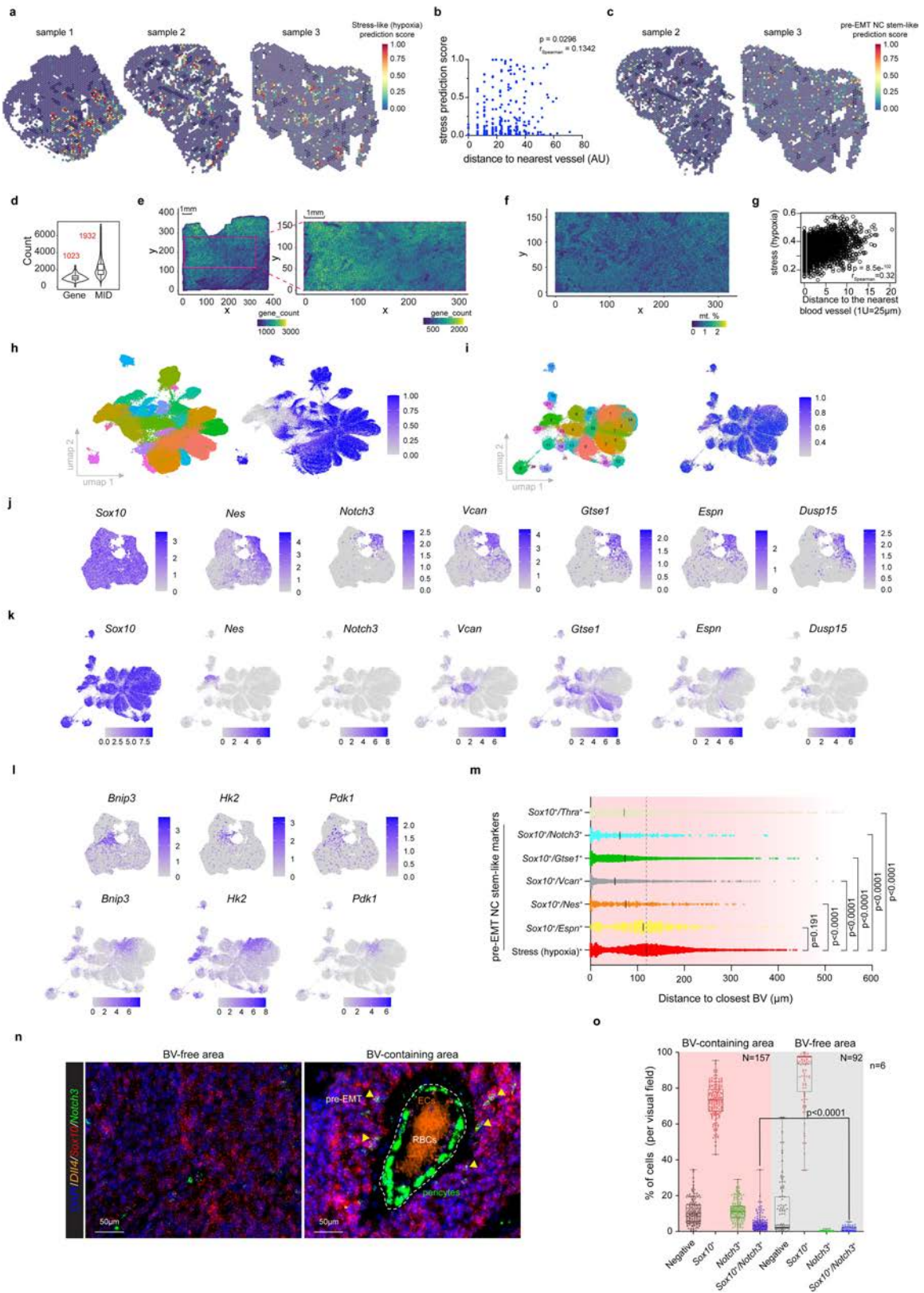
Extended Data Fig. 4 | Clone size distributions are consistent with the hierarchical model. **a**, Cluster-cluster distance correlation indicating a high likelihood that clusters of a given colour are found near clusters of the same colour for distances below 100 μm . This threshold, indicated by a dashed line, was then used in the association of clones. Solid line and shaded area correspond to mean and $\pm\text{SEM}$ for $n = 5$ biological repeats. **b–e**, Cumulative distribution (CDF) of clone sizes for YFP⁺ and RFP⁺ cells in samples 2-5 (for number of clones per sample see Supplementary Table 5) Sample 1 is presented in Fig. 2f. The dashed black lines correspond to the bi-exponential fits of the data, as predicted by the hierarchical model, for each dataset we show the R-squared (R^2) and standard error of the fit (S) of the theoretical CDFs to the data. **f**, Sensitivity of the stem cell expansion rate, cycling rate and stem cell

fraction to different choices of the stem cell symmetric division probability, r . The vertical dotted line indicates the value $r = 0.75$ used here to estimating the model parameters (see Supplementary Table 5). **g–k**, Comparison of the empirical CDFs of clone sizes for each of the $n = 5$ biological repeats and the corresponding distributions and SD obtained from performing 10,000 stochastic simulations of the two-compartment stem-progenitor cell model using the parameters in Supplementary Table 5. The p-values from two-sample Kolmogorov-Smirnov tests comparing the empirical and numerical distribution of clone sizes are shown. In **f** and **i**, the RFP channel of sample 3 is not shown as it was considered to be below the threshold of clonality. For Extended Data Fig. 5 see Supplementary Note in Supplementary Information).



Extended Data Fig. 5 | Hierarchical melanoma growth is independent of the adaptive immune system. **a**, Schematic representation of the generated melanoma mouse model transplanted in immunocompromised mice (*Foxn1^{null}*). Schematic made with Biorender.com. **b**, Tumour growth kinetics (mm^3) of individual tumours in immunodeficient mice (yellow), and corrected mean obtained from fitting an exponential growth to each individual sample (black curve). Dashed lines indicate tumour duplication times. Dotted red curve refers to the mean growth kinetics extracted from Fig. 2b. **c**, Confocal images showing Confetti labelling efficiency in melanoma tumours 3 days after the administration of different doses of TAM in order to achieve the optimal dose to perform clonal analyses. Representative images from $n = 3$ independent

tumours. **d**, Confocal image showing Confetti labelling of melanoma cells 5 days after TAM administration (0.5 mg) in immunodeficient background. Representative image from $n = 5$ independent tumours. **e**, Violin plot depicting the proportion of labelled melanoma cells expressing each Confetti fluorophore 5 days after TAM administration (0.5 mg). Six melanoma tumours (two sectional area of each) were analysed. Black line represents median and grey lines the 25th to 75th percentile. **f**, Confocal images of melanoma tumours in immunodeficient background exhibiting Confetti labelling 5 days after initial induction (1.5-fold tumour increase) and at relative growth of 10-fold upon single low dose intraperitoneal Tamoxifen administration (0.5 mg). Representative images from $n = 3$ independent tumours.



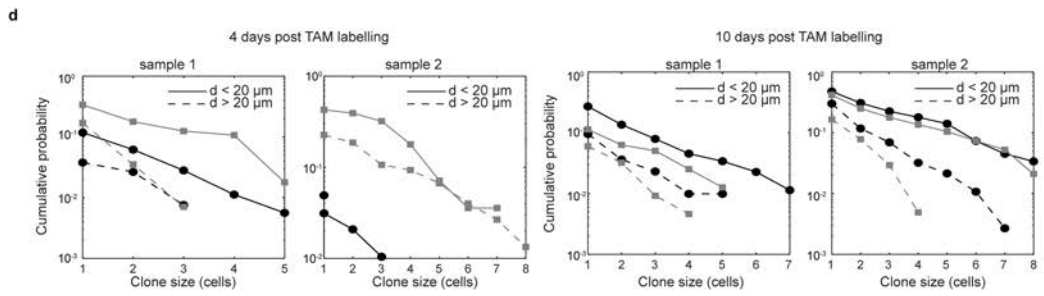
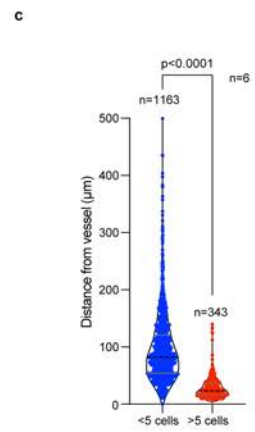
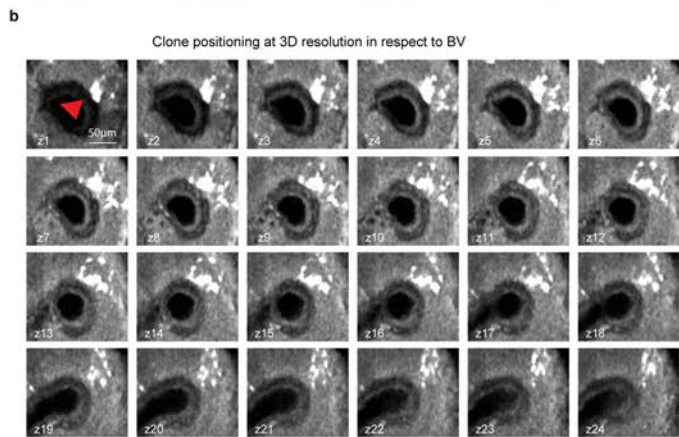
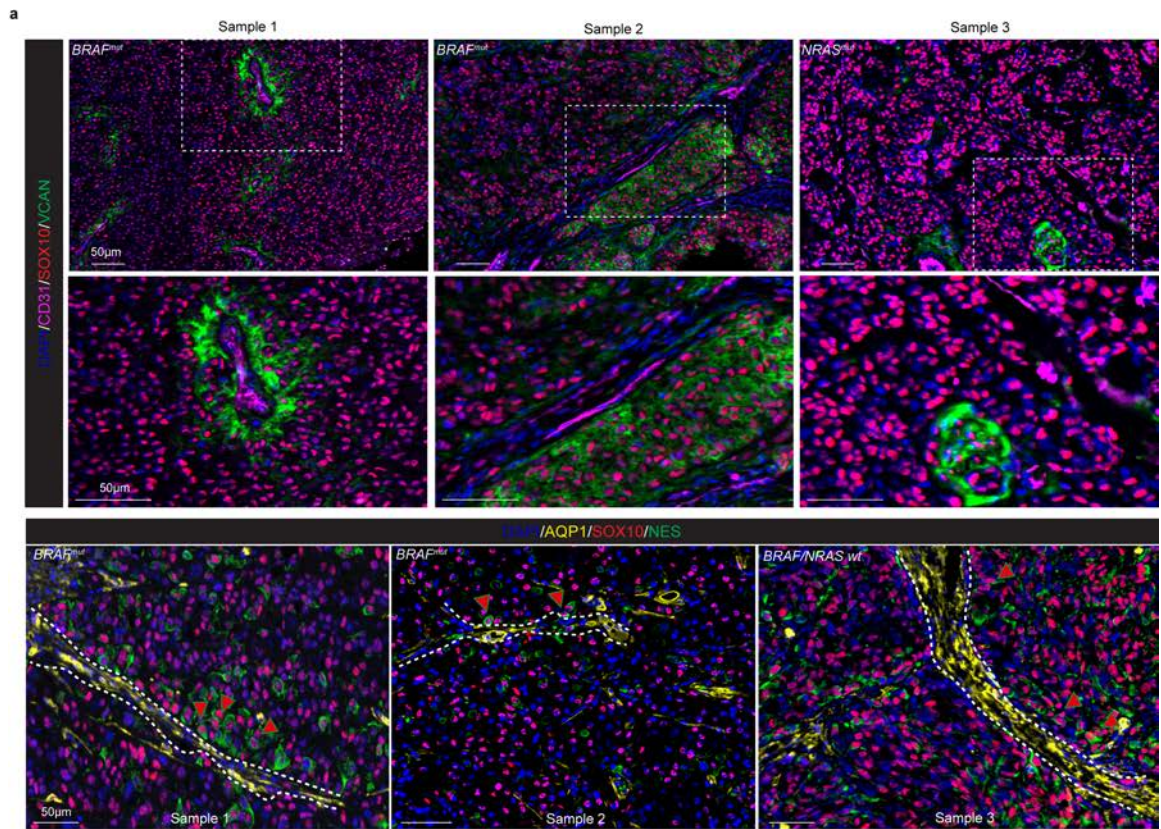
Extended Data Fig. 6 | See next page for caption.

Article

Extended Data Fig. 6 | Spatially mapping melanoma heterogeneity.

a, Spatially resolved quantification of stress-like (hypoxia) state (prediction score) by label transfer of scRNA-seq data onto Visium spots (sample 1,2,3). **b**, Scatter plot shows a positive correlation (Spearman) between the stress-like (hypoxia) activity score and the distance to the nearest BV (Fisher's exact test, two-tailed p value). **c**, Spatially resolved quantification of pre-EMT NC stem-like state (prediction score) by label transfer of scRNA-seq data onto Visium spots (sample 2,3). **d**, Violin plots and box plots showed the number of Stereo-seq detected genes (left) and Molecular Identifier (MID) (right) per bin50 (25 μ m diameter). The middle horizontal line of the boxplot represents the median. **e**, Gene count visualization of Stereo-seq data. **f**, ROI coloured by percentage of mitochondrial gene count (bin50). **g**, Scatter plot shows correlation (Spearman) of stress-like (hypoxia) activity (AUCell score) and distance to closest blood vessel per bin based on Stereo-seq bin50 data (Fisher's exact test, two-tailed p value). **h**, UMAP of all segmented cells (170k) from molecular cartography (see Fig. 3f), coloured by Seurat cluster and melanoma (melanocytic state) gene signature activity (AUCell score). **i**, UMAP of malignant subset (109k) from molecular cartography, coloured by Seurat

cluster and melanoma (melanocytic state) gene signature activity (AUCell score). **j**, Expression of pre-EMT NC stem-like cell markers assessed by scRNA-seq. **k**, Expression of pre-EMT NC stem-like cell markers assessed by Molecular Cartography. **l**, Expression of stress-like (hypoxia) cell markers as assessed by scRNA-seq (upper panels) and Molecular Cartography (lower panels). **m**, Horizontal histogram showing median distance (black line) to the nearest blood Vessel (BV) for all cells annotated as stress-like (hypoxia) or expressing *Sox10* and one of the indicated pre-EMT NC stem-like markers. Exact p values are indicated. **n**, Representative confocal image showing mRNA expression of the indicated genes, as detected by RNAscope, in blood vessel (BV) free and containing areas. Yellow arrowheads indicate the presence of cells positive for both *Sox10* (red) and *Notch3* (green). Endothelial Cells (*Dll4*⁺) are highlighted in orange. RBCs, Red Blood Cells. **o**, Quantification of **m** (n = 6; p < 0.0001). Boxes extend from the 25th to 75th percentile. The middle line represents the median. Whiskers represent min to max values. In panels **m** and **o** significance was assessed by an unpaired nonparametric, two-tailed Mann-Whitney Test (approximate p value, p < 0.0001).

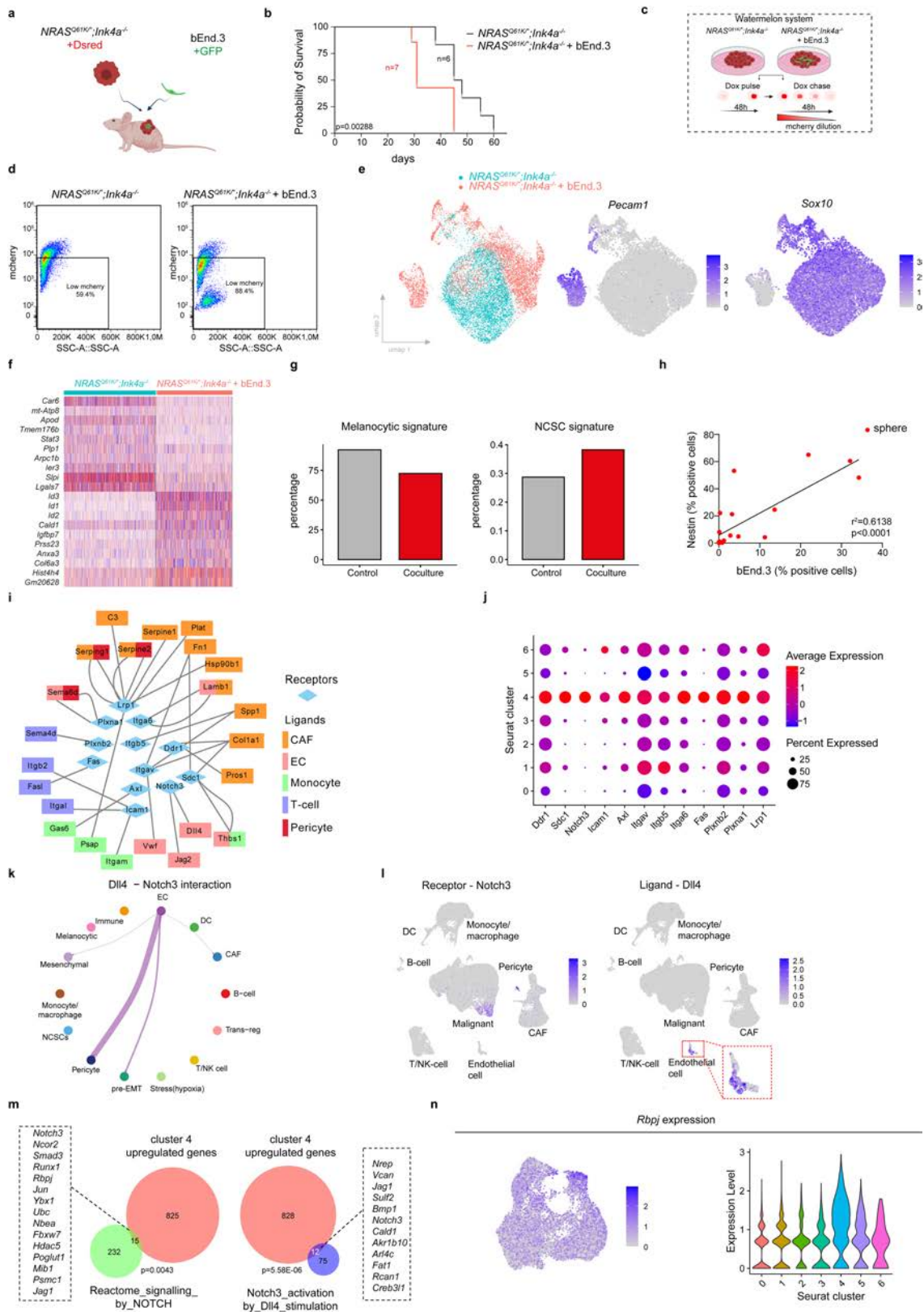


Extended Data Fig. 7 | See next page for caption.

Article

Extended Data Fig. 7 | Mapping the melanoma perivascular niche in human primary melanomas. a. Confocal image of immunostaining of human primary melanoma lesions for CD31, SOX10, VCAN (upper panel, 3 representative lesions from 5 tumours) or CD31, SOX10, NES (lower panel, 3 representative lesions from 7 tumours). The main driver mutations are indicated. **b.** Spatial distribution of Confetti clones in respect to vessels. Panel of xy images of a clone (indicated with the red arrowhead) in close proximity to the vessel at indicated z-stack positions (z1-z24). V corresponds to the vessel. **c.** Violin plot depicting 2D quantification of subclones categorized in two groups based on their size and their spatial distance (μm) from the BV (visualized by AQP1 staining,

$n = 6$; $p < 0.0001$). Dashed line represents median and grey lines the 25th to 75th percentile. Significance was by an unpaired nonparametric, two-tailed Mann-Whitney Test. **d.** Cumulative distribution of clone sizes for clones directly in contact with the vasculature (distance $< 20 \text{ m}$, solid lines) and clones detached from it (distance $\geq 20 \text{ m}$, dashed lines) for RFP (black circles) and YFP (grey squares) channels, obtained from short-term clonal labelling of (left) 4 days and (right) 10 days post TAM, where the vasculature was segmented after staining with CD31 staining in $n = 2$ biological repeats for each time-point (shown separately).



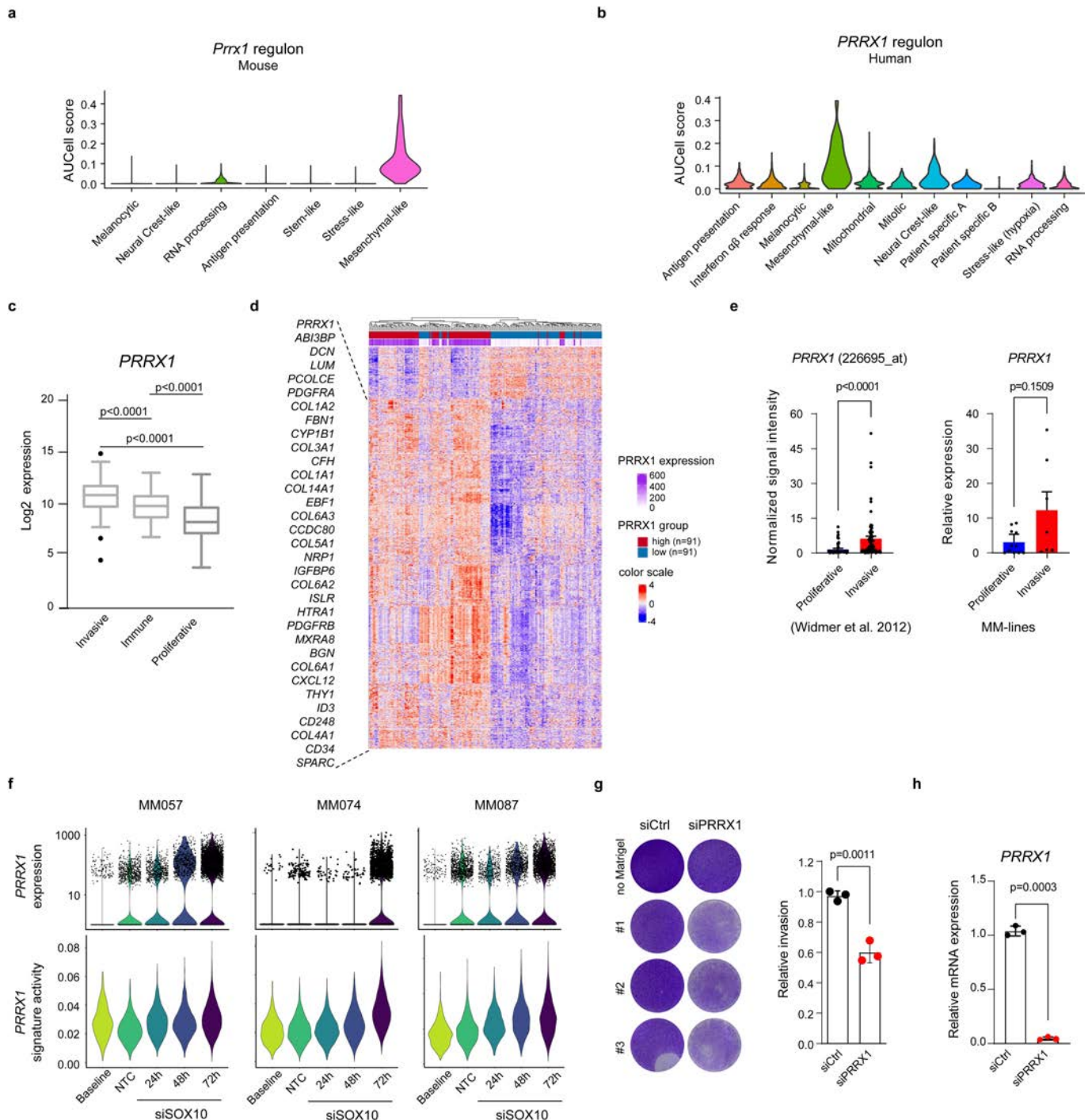
Extended Data Fig. 8 | See next page for caption.

Article

Extended Data Fig. 8 | Melanoma-Endothelial cell heterotypic interaction promotes growth and induction of the pre-EMT NC stem-like phenotype.

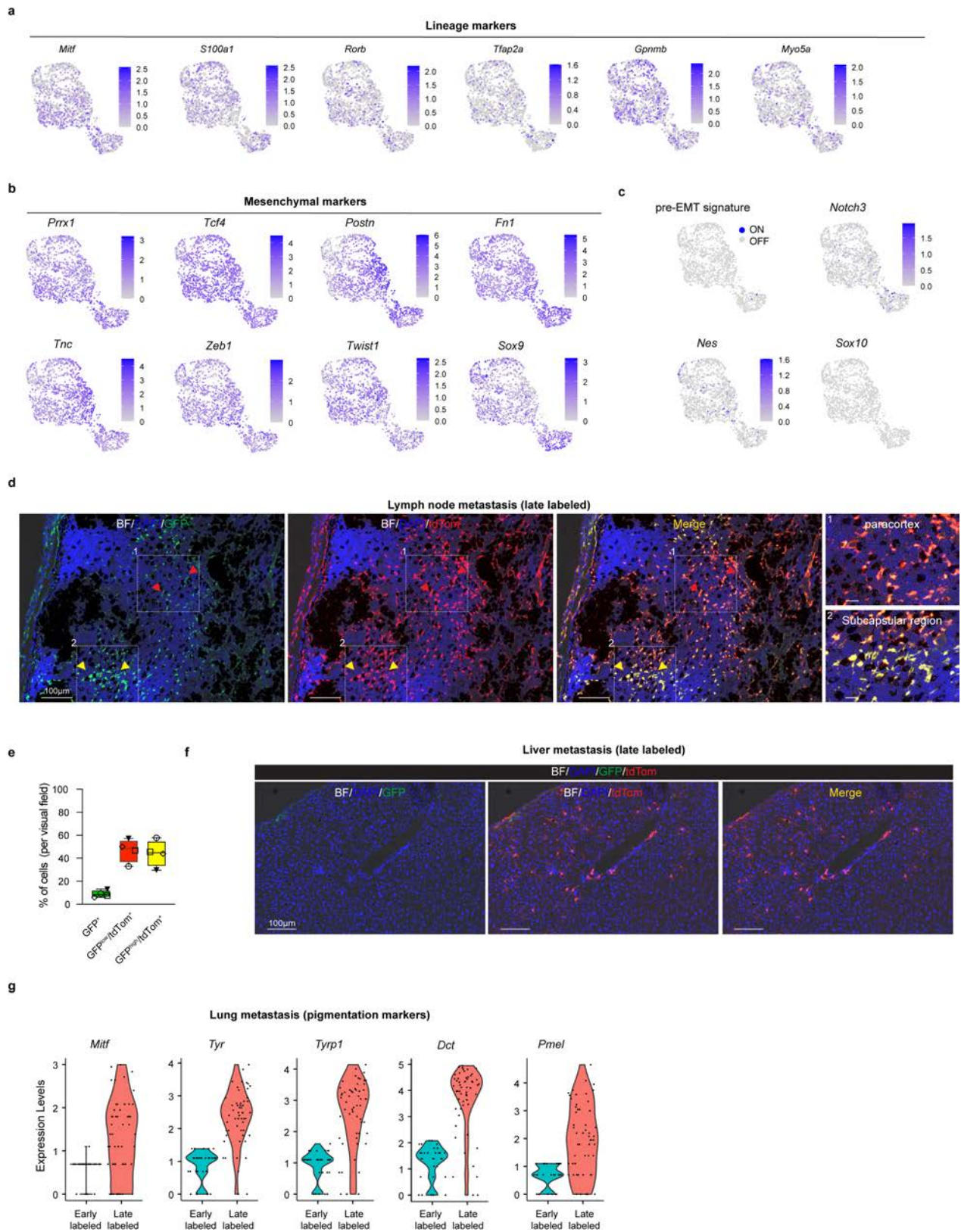
a, Schematic representation of Fig. 3i. **b**, Kaplan-Meier survival curves from log-rank (Mantel-Cox) test of mice described in **a** ($p = 0.00288$, n is indicated in the graph). **c**, Schematic representation of *in vitro* assays using the Watermelon system. **d**, Representative FACS profiles from Fig. 3j and experiment described in **c**. Percentages of low mcherry (mNeon-positive) populations. **e**, *NRAS*^{Q61K/+}; *Ink4a*^{-/-} cells cultured either alone or in the presence of bEnd.3 cells for 48h and processed for scRNA-seq. Left, UMAP by sample identity; middle, expression of the endothelial cell marker *Pecam1*; and right, pan-melanoma marker *Sox10*. **f**, Heatmap showing the overall transcriptional reprogramming effect observed following exposure of *NRAS*^{Q61K/+}; *Ink4a*^{-/-} melanoma cells to bEnd.3 endothelial cells. **g**, Percentage of melanoma cells positive for the melanocytic and Neural Crest-like signatures (binary AUCell score). **h**, Melanospheres of *NRAS*^{Q61K/+}; *Ink4a*^{-/-} cells grown in the presence of GFP-labelled bEnd.3 ECs for 10 days and the percentage of Nestin-positive cells was correlated with the amount of bEnd.3/GFP-positive cells. Linear regression test was used for statistical significance ($n = 19$). **i**, Predicted cell-to-cell interactions based on known ligand-receptor pairs between tumour

microenvironment populations (ligands) and the pre-EMT NC stem-like malignant cells (receptors) in scRNA seq data from mouse tumours as inferred by NicheNet. **j**, Dotplot showing gene expression intensities of selected receptors over the different Seurat clusters. **k**, Circos plot illustrating *Dll4-Notch3* predicted interaction between cell types in scRNA seq data from mouse tumours and inferred by CellChat. The edge width is proportional to the prediction score. Note the predicted interaction of pre-EMT NC stem-like state with ECs. **l**, UMAP highlighting the specific expression of the ligand *Dll4* in ECs and the receptor *Notch3* in subpopulation of malignant cells. **m**, Left panel shows venn diagram highlighting the overlap of the pre-EMT NC stem-like cell state (cluster 4) upregulated genes with NOTCH signalling signature (Reactome). Right panel shows venn diagram highlighting the significant overlap of the pre-EMT NC stem-like cell state (cluster 4) upregulated genes with a Notch3 activation signature³¹. Hypergeometric distribution test was used for statistical analysis. P values are indicated in each Venn diagram. **n**, *Rbpj* expression in the malignant cluster of scRNA data from *NRAS*^{Q61K/+}; *Ink4a*^{-/-} lesions projected either as UMAP (left panel) or as violin plot (right panel) for each malignant transcriptional state. Schematic in **a** and **c** made with Biorender.com.



Extended Data Fig. 9 | PRRX1 is a master regulator of the mesenchymal-like transcriptional program. **a**, Violin plots depict conserved *Prrx1* regulon activity scores (AUCell) across mouse Seurat clusters. **b**, Violin plots depict conserved *PRRX1* regulon activity scores (AUCell) across human Seurat clusters. **c**, *PRRX1* expression in $n = 375$ TCGA_SKCM patients stratified as invasive ($n = 123$), immune-related ($n = 116$) and proliferative ($n = 136$) phenotypes based on their gene expression profile described previously³⁵. Box plots summarize the values per phenotypic group and show the median. Boxes extend from the 25th to 75th percentiles, whiskers and outliers were plotted according to the Tukey method. Significance was assessed by an unpaired nonparametric, two-tailed Mann-Whitney Test (approximate p value, $p < 0.0001$). **d**, Heatmap generated using the TCGA database illustrating the gene expression profile of patients with *PRRX1* high and low expression (20th percentile cut-off). Genes from the conserved *PRRX1* regulon are co-expressed together with *PRRX1*. **e**, Left panel, *PRRX1* expression (P226695_at) in invasive

($n = 71$) and proliferative ($n = 81$) melanoma cell lines as previously described³⁶. Error bars represent \pm SEM. Significance was assessed by an unpaired nonparametric, two-tailed Mann-Whitney Test (approximate P value, $p < 0.0001$). Right panel, qPCR analysis for *PRRX1* in short term melanoma cell lines categorized as proliferative ($n = 11$) and invasive ($n = 7$) based on their gene expression profile). Error bars represent \pm SEM. Significance was assessed by unpaired nonparametric two-tailed Student's t -test. ($p = 0.1509$). **f**, *PRRX1* expression (upper panel) and signature activity (lower panel) in short term proliferative/melanocytic melanoma cell lines (MM057, MM074 and MM087) transfected with SOX10 siRNA or non-targeting control. Baseline refers to the non-transfected melanoma cell lines. **g**, Left panel, Matrigel-invasion assay upon silencing of *PRRX1* in MM099 cells. Right panel, quantification ($n = 3$; $p = 0.0011$). **h**, Relative mRNA expression of *PRRX1* upon siPRRX1 ($n = 3$; $p = 0.0003$). In **g** and **h** significance was assessed by unpaired two-tailed Student's t -test.



Extended Data Fig. 10 | See next page for caption.

Extended Data Fig. 10 | Reprogramming of *Prrx1*⁺ melanoma cells during metastatic spreading. **a**, Expression of melanocytic lineage markers in malignant FACS-sorted tdTomato⁺ cells isolated from a primary melanoma lesion of Met-track mice, 2 days (early labelled) post-TAM. **b**, Expression of *Prrx1* and well-established melanoma mesenchymal-like markers in cells described in **a**. **c**, Expression of pre-EMT NC stem-like cell markers and activity (AUC_{cell} score) of the pre-EMT NC stem-like cell signature in cells described in **a**. **d**, Confocal image of a lymph node metastasis 4 weeks post-TAM. Cells positive for both GFP and tdTomato reporters (subcapsular region) as well as tdTomato⁺ cells expressing lower to undetectable levels of GFP. Black regions correspond

to the pigmented melanoma cells. BF, Bright Field. Representative images from 5 different tumours. **e**, Box plots showing the percentage of tdTomato⁺/GFP^{high} versus and tdTomato⁺/GFP^{low} cells in lymph nodes (n = 4 mice). Boxes extend from the 25th to 75th percentile. The middle line represents the median. Whiskers represent min to max values. **f**, Confocal image of single tdTomato⁺ (and GFP^{low}) cells in the liver of a Met-Track mouse 4 weeks post-TAM. Representative image from 2 different tumours. **g**, Violin plots of *Mitf* expression and pigmentation genes in FACS-sorted tdTomato⁺ fraction isolated from lung metastases 2 days (early labelled) and 30-days (late labelled) post-TAM administration.

Reporting Summary

Nature Research wishes to improve the reproducibility of the work that we publish. This form provides structure for consistency and transparency in reporting. For further information on Nature Research policies, see our [Editorial Policies](#) and the [Editorial Policy Checklist](#).

Statistics

For all statistical analyses, confirm that the following items are present in the figure legend, table legend, main text, or Methods section.

- | n/a | Confirmed |
|-------------------------------------|--|
| <input type="checkbox"/> | <input checked="" type="checkbox"/> The exact sample size (<i>n</i>) for each experimental group/condition, given as a discrete number and unit of measurement |
| <input type="checkbox"/> | <input checked="" type="checkbox"/> A statement on whether measurements were taken from distinct samples or whether the same sample was measured repeatedly |
| <input type="checkbox"/> | <input checked="" type="checkbox"/> The statistical test(s) used AND whether they are one- or two-sided
<i>Only common tests should be described solely by name; describe more complex techniques in the Methods section.</i> |
| <input checked="" type="checkbox"/> | <input type="checkbox"/> A description of all covariates tested |
| <input checked="" type="checkbox"/> | <input type="checkbox"/> A description of any assumptions or corrections, such as tests of normality and adjustment for multiple comparisons |
| <input type="checkbox"/> | <input checked="" type="checkbox"/> A full description of the statistical parameters including central tendency (e.g. means) or other basic estimates (e.g. regression coefficient) AND variation (e.g. standard deviation) or associated estimates of uncertainty (e.g. confidence intervals) |
| <input type="checkbox"/> | <input checked="" type="checkbox"/> For null hypothesis testing, the test statistic (e.g. <i>F</i> , <i>t</i> , <i>r</i>) with confidence intervals, effect sizes, degrees of freedom and <i>P</i> value noted
<i>Give P values as exact values whenever suitable.</i> |
| <input checked="" type="checkbox"/> | <input type="checkbox"/> For Bayesian analysis, information on the choice of priors and Markov chain Monte Carlo settings |
| <input checked="" type="checkbox"/> | <input type="checkbox"/> For hierarchical and complex designs, identification of the appropriate level for tests and full reporting of outcomes |
| <input type="checkbox"/> | <input checked="" type="checkbox"/> Estimates of effect sizes (e.g. Cohen's <i>d</i> , Pearson's <i>r</i>), indicating how they were calculated |

Our web collection on [statistics for biologists](#) contains articles on many of the points above.

Software and code

Policy information about [availability of computer code](#)

Data collection

Image acquisition
 -ZEISS Axio Scan.Z1
 -Vectra® Polaris™
 -Nikon C2
 -Zeiss LSM 880 Airyscan
 - IncuCyte Zoom (Sartorius)

FACS
 -BD FACSAria fusion sorter (FACSDiva 9.0.1)
 -SONY MA900 (MA900 software)
 -BD LSRFortessa™ X-20 (FACSDiva 9.0.1)

Data analysis

Image processing:
 -Fiji (version 1.53p)
 - Qupath 0.2.3 with stardist
 - Zeiss ZEN 2.3

Bioinformatics:
 -pySCENIC v.0.9.19
 -Nexflow v. 20.04.1
 -R version 3.6.1 / 4.0.3
 -CellRanger v.3.1.0
 -SpaceRanger v.1.0.0
 -DoubletFinder R v.2.0.2

-Harmony R v.1.0
 -Seurat R v.3.1.5
 -AUCell R v.1.8.0
 -Nichenetr R v.0.1.0
 -hypeR R v.1.5.4
 -honeyBADGER R v.0.1
 -CellChat R v.1.1.3

Graphs and data analysis:

-GraphPad Prism 9.2.0
 -Excel 2016

FACS analysis

-FlowJo (V10.7.1 for Mac and v.10.7.2 for windows; Becton, Dickinson & Company; 2021)

Code

-Code for analysis of 3D clone data, implemented on MATLAB R2020a, The MathWorks, Inc., Natick, Massachusetts, USA, available on a public Github repository: https://github.com/ibordeu/scripts_Karras_et_al_2022_git
 -Scripts and annotation files for the study have been deposited on github at: <https://github.com/MarineLab/Karras-et-al>

For manuscripts utilizing custom algorithms or software that are central to the research but not yet described in published literature, software must be made available to editors and reviewers. We strongly encourage code deposition in a community repository (e.g. GitHub). See the Nature Research [guidelines for submitting code & software](#) for further information.

Data

Policy information about [availability of data](#)

All manuscripts must include a [data availability statement](#). This statement should provide the following information, where applicable:

- Accession codes, unique identifiers, or web links for publicly available datasets
- A list of figures that have associated raw data
- A description of any restrictions on data availability

Raw sequencing data of scRNAseq and spatial transcriptomics (Visium and Stereo-seq) are deposited to GEO under accession number GSE207592. Processed count matrices (scRNAseq and Visium) are available at: <https://marinelab.sites.vib.be/en>. Molecular cartography data are available at Zenodo: <https://zenodo.org/record/6856193#.Ytj-fnZBz-g>.

Field-specific reporting

Please select the one below that is the best fit for your research. If you are not sure, read the appropriate sections before making your selection.

Life sciences Behavioural & social sciences Ecological, evolutionary & environmental sciences

For a reference copy of the document with all sections, see nature.com/documents/nr-reporting-summary-flat.pdf

Life sciences study design

All studies must disclose on these points even when the disclosure is negative.

Sample size	Samples sizes were not pre-determined based on statistical power calculations but were based on our experience with these assays. All in vivo experiments included at least 3 mice and the results were reliably reproduced. The previous experiences refer to: success of tumor engraftment, efficient labeling of confetti tumors, frequency of melanoma development and metastasis in GEMMs, efficient engraftment of injected melanoma and endothelial cells.
Data exclusions	Mice with engrafted tumors that failed to grow were excluded from the study. The mice that received tamoxifen injection in the confetti background and the clonal density was too high were excluded. The clonal density was assessed by confocal imaging and quantification using Qupath. For single cell analysis cells were excluded based on a QC filter described in the methods section.
Replication	All attempts at replication were reliably reproduced. Measures were taken individually from each animal within the experiment. Each animal was considered as a biological replicate. Mice with engrafted tumors that failed to grow were excluded from the study. The mice that received tamoxifen injection in the confetti background and the clonal density was too high were excluded. To assess clonality using Confetti mice the experiments were reproduced to at least 3 different cohorts of mice. Co-injection experiments were really reproduced in at least two independent experiments. The clonal density was assessed by confocal imaging and quantification using Qupath. All in vitro experiments co-culturing melanoma and endothelial cells have been reproduced in at least two independent experiments. All -omics data (RNA-seq, spatial transcriptomics) were performed as following: For single cell RNA sequencing experiments the following numbers of mice were used according to the mouse model: - 5 mice from Tyr::NRASQ61K ⁺ ; Ink4a ^{-/-} ; Tyr::CreERT2 ⁺ ; Rosa26-LSL-Confetti ^{+/+} allograft model - 2 mice from Tyr::CreERT2 ⁺ ; BRafCA ^{+/+} ; Pten ^{l/l} ; ROSA26LSL-tdTomato/LSL-tdTomato model - 2 from Prx1::CreER-GFP; Tyr-NRASQ61K ⁺ ; Ink4a ^{-/-} ; ROSA26LSL-tdTomato/LSL-tdTomato Spatial transcriptomic analyses using unbiased or targeted approaches was performed in mice with Tyr::NRASQ61K ⁺ ; Ink4a ^{-/-} ; Tyr::CreERT2 ⁺ ; Rosa26-LSL-Confetti ^{+/+} background and the following numbers of mice were used: - 3 tumors from 3 different mice for 10x visium platform - 1 tumor from 1 mouse for Stereo-seq - Three sections from two tumor samples were used for Molecular Cartography

For the in vitro co-culture single cell RNAseq analyses data refer single replicates.

Randomization The experiments were not randomized. The mice included in this study were selected according to their correct genotype.

Blinding There was no case/control design. For clonality experiments engrafted tumors were TAM induced, followed during growth, and sacrificed at different tumor sizes; blinding was not applicable as all mice had the same genotype. Similarly for dual incorporation experiments. For PRRX1 tracing, cohort of mice have been generated and followed until melanomas developed. Subsequently, mice were TAM induced and sacrificed in different time points. The traced mice had the same genetic background and blinding was not possible. For co-injection experiment blinding was partially possible. The same investigator prepared the samples and injected them in mice and another investigator followed the growth kinetics without prior knowledge of the injected mouse groups.

Reporting for specific materials, systems and methods

We require information from authors about some types of materials, experimental systems and methods used in many studies. Here, indicate whether each material, system or method listed is relevant to your study. If you are not sure if a list item applies to your research, read the appropriate section before selecting a response.

Materials & experimental systems

- | n/a | Involvement in the study |
|-------------------------------------|---|
| <input type="checkbox"/> | <input checked="" type="checkbox"/> Antibodies |
| <input type="checkbox"/> | <input checked="" type="checkbox"/> Eukaryotic cell lines |
| <input checked="" type="checkbox"/> | <input type="checkbox"/> Palaeontology and archaeology |
| <input type="checkbox"/> | <input checked="" type="checkbox"/> Animals and other organisms |
| <input type="checkbox"/> | <input checked="" type="checkbox"/> Human research participants |
| <input checked="" type="checkbox"/> | <input type="checkbox"/> Clinical data |
| <input checked="" type="checkbox"/> | <input type="checkbox"/> Dual use research of concern |

Methods

- | n/a | Involvement in the study |
|-------------------------------------|--|
| <input checked="" type="checkbox"/> | <input type="checkbox"/> ChIP-seq |
| <input type="checkbox"/> | <input checked="" type="checkbox"/> Flow cytometry |
| <input checked="" type="checkbox"/> | <input type="checkbox"/> MRI-based neuroimaging |

Antibodies

Antibodies used

The following primary antibodies were used (antibody, dilution, provider, Catalogue number):

- anti-GP100 (1:400, Abcam, #ab137078)
- anti-MITF (1:200, Sigma-Aldrich, #HPA003259)
- anti-AQP1 (1:2000, Millipore, #AB2219)
- anti-CD31/PECAM-1 (1:200, Dianova, #DIA-310)
- anti-MLANA (1:200, Sigma-Aldrich, HPA048662)
- anti-NES (1:100, Abcam, #ab81462)
- anti-BrdU (1:100, Abcam, #ab6326)
- anti-SOX10 (1:100, Invitrogen, #703439) for mouse samples
- anti-SOX10 (1 µg/ml, SCBT, #sc-365692) for human samples using MILAN platform
- anti-SOX10 (1:200, R&D Systems, #AF2864) for human samples using OPAL staining approach
- anti-NOTCH3 (1:100, Abcam, #ab23426)
- anti-VCAN (0.2 µg/ml, Sigma-Aldrich, #HPA004726)
- anti-CD31 (1 µg/ml, LSBio; #LS-C173974)

The following secondary antibodies were used:

- Donkey-anti-Rat IgG (H+L), Alexa Fluor 488 (1:400, Thermofisher Scientific, #A-21208)
- Donkey-anti-Rabbit IgG (H+L), Alexa Fluor 647 (1:400, Thermofisher Scientific, #A31573)
- Goat-anti-Rat IgG (H+L), Alexa Fluor 647 (1:400, Thermofisher Scientific, #A21247)

For FACs analyses in Prrx1::CreER-GFP;Tyr-NRASQ61K^o;Ink4a^{-/-};ROSA26RLSL-tdTomato/LSL-tdTomato, negative selection of aSMA⁺ population was achieved by using anti-alpha-Smooth Muscle Actin (1A4), eFluor 660 (1:500, ThermoFisher Scientific, 50-9760-82).

Validation

All the antibodies in this study were used in immunofluorescence approaches. All commercial antibodies used were optimized following manufacturer's instructions (see websites) and different dilutions if needed. Negative controls (only secondary antibodies) were also included. The following primary antibodies have been validated by the manufacturer:

- anti-GP100 (1:400, Abcam, #ab137078), <https://www.abcam.com/melanoma-gp100-antibody-ep48632-ab137078.html>
- anti-MITF (1:200, Sigma-Aldrich, #HPA003259), <https://www.sigmaaldrich.com/BE/en/product/sigma/hpa003259>
- anti-AQP1 (1:2000, Millipore, #AB2219), https://www.merckmillipore.com/BE/fr/product/Anti-Aquaporin-1-Antibody,MM_NF-AB2219?ReferrerURL=https%3A%2F%2Fwww.google.com%2F
- anti-CD31/PECAM-1 (1:200, Dianova, #DIA-310), <https://www.dianova.com/en/shop/dia-310-anti-cd31-mssw-from-rat-sz31-unconj-for-mouse-ffpe-tissue/>
- anti-MLANA (1:200, Sigma-Aldrich, HPA048662), <https://www.sigmaaldrich.com/BE/en/product/sigma/hpa048662>
- anti-NES (1:100, Abcam, #ab81462), <https://www.abcam.com/nestin-antibody-7a3-ab81462.html>
- anti-BrdU (1:100, Abcam, #ab6326), <https://www.abcam.com/brdu-antibody-bu175-icr1-proliferation-marker-ab6326.html>
- anti-SOX10 (1:100, Invitrogen, #703439), <https://www.thermofisher.com/antibody/product/SOX10-Antibody-clone-5H7L26-Recombinant-Monoclonal/703439>
- anti-SOX10 (1 µg/ml, SCBT, #sc-365692), <https://www.scbt.com/p/sox-10-antibody-a-2?requestFrom=search>
- anti-SOX10 (1:200, R&D Systems, #AF2864), https://www.rndsystems.com/products/human-sox10-antibody_af2864

- anti-NOTCH3 (1:100, Abcam, #ab23426), <https://www.abcam.com/notch3-antibody-ab23426.html>
 - anti-VCAN (0.2 µg/ml, Sigma-Aldrich, #HPA004726), <https://www.sigmaaldrich.com/BE/en/product/sigma/hpa004726>
 - anti-CD31 (1 µg/ml, LSBio; #LS-C173974), <https://www.lsbio.com/antibodies/ihc-plus-pecam-1-antibody-cd31-antibody-clone-oti2c6-ihc-wb-western-ls-b16850/856292>
 - anti-alpha-Smooth Muscle Actin (1A4), eFluor 660, <https://www.thermofisher.com/antibody/product/Alpha-Smooth-Muscle-Actin-Antibody-clone-1A4-Monoclonal/50-9760-82>

Eukaryotic cell lines

Policy information about [cell lines](#)

Cell line source(s)	Melanoma cell lines were received from Prof. G. Ghanem, LOCE-institut J. Bordet, Université Libre de Bruxelles. Melanoma cell line from Tyr::NRASQ61K/°; Ink4a-/-;Tyr::CreERT2/°;Rosa26-LSL-Confetti+/+ GEM mice was generated and validated by qPCR using melanocytic markers. Bend3 cells were provided by M. Mazzone (VIB-CCB, Belgium). HEK293 FT cell line was used for lentiviral particle production to transduce melanoma and Bend3 cells.
Authentication	Authentication was ensured validating the cell lines by qPCR for melanocytic markers, or phenotyped using cell state specific gene signatures (PRO and INV).
Mycoplasma contamination	All cell lines tested were negative for mycoplasma
Commonly misidentified lines (See ICLAC register)	No commonly misidentified lines were used in this study.

Animals and other organisms

Policy information about [studies involving animals](#); [ARRIVE guidelines](#) recommended for reporting animal research

Laboratory animals	Animal model: Mus musculus Strains: C57BL/6JAX, Foxn1nu, Tyr::CreERT2, Tyr-NrasQ61K/+, Ink4a-/-, R26RLSL-tdTomato, R26RLSL-confetti, Prrx1::CreER-IRES2-EGFP, BRafCA/+; Pten/l. Animals were analyzed at adult stages. For clonality experiments using Confetti model, 8-to-10 week old female mice were used. For tracing experiments in Prrx1::CreER-GFP;Tyr-NRASQ61K/°;Ink4a-/-;ROSA26RLSL-tdTomato/LSL-tdTomato model, mice develop melanomas in average 8-10 months after birth. Once melanomas were developed, mice started to be traced in male and female animals. For subcutaneous injections (Foxn1nu background) of melanoma and endothelial cells, 8-to-10 week old female mice have been used. For melanoma induction in the Tyr::CreERT2;BRafV600E/+;Pten/l background, 6-to-12 week old male and female mice were used. Animals were housed in a controlled environment with 14/10hour light/dark cycles, standard diet and water ad libitum.
Wild animals	The study didn't involve wild animals.
Field-collected samples	The study did not involved samples collected from the field
Ethics oversight	All tissue material was collected before final ethical endpoint. All mice colonies were maintained in a certified animal facility in accordance with European guidelines. All experiments involving animals were reviewed and approved by the Institutional Animal Care and Research Advisory Committee of University of Leuven, Belgium. The ethical approval project numbers are indicated in the relevant Methods section.

Note that full information on the approval of the study protocol must also be provided in the manuscript.

Human research participants

Policy information about [studies involving human research participants](#)

Population characteristics	Gender: 9 males, 12 females Age (years): median 66 (range 34-82) Histologic subtype: - Superficial spreading (n = 7) - Nodular (n = 8) - Acral lentiginous (n = 1) - Desmoplastic (n = 1) - Naevoid (n = 1) - Unknown (n = 4) Prior treatment: - Treatment naïve (n = 20) - PD-1 (n = 1) - Chemotherapy (n = 1) - MAPK inhibition (n = 1) Mutational status: - BRAF mutated (n = 14) * V600E (n = 11) * Other V600 (n = 2) * Non V600 (n = 3)
----------------------------	---

- NRAS mutated (n = 5)
 - NF1 mutated (n = 2)
 - Triple wild type (n = 1)
 - Unknown (n = 3)
 Biopsy site:
 - Lymph node (n = 14)
 - Skin (n = 4)
 - Subcutis (n = 4)

Recruitment

Patients biopsies were collected as part of a non-interventional single-center prospective study investigating transcriptomic changes upon immune checkpoint inhibition (Prospective Serial biopsy collection before and during immune-checkpoint inhibitor therapy in patients with malignant melanoma (SPECIAL)). Patients presenting at our institution (UZ Leuven/ University Hospitals Leuven) with locally advanced or metastatic melanoma (AJCC 8th ed. st. III-IV) amendable for serial biopsy prior and early after cycle 1 of treatment with anti-PD1 (nivolumab or pembrolizumab). Immune checkpoint inhibitor therapy was allowed in first line or in second line after failure of MAPK inhibitor therapy. Combination with anti-CTLA4 (ipilimumab) was allowed in neo-adjuvant setting. Prior immune checkpoint inhibition in adjuvant setting was allowed if last dosage was longer than 6 months prior to inclusion. Biopsies were preferentially taken from easily accessible sites (skin, subcutis, lymph node) rather than visceral sites (liver, lung, brain). For that reason this study is mainly focused on skin or lymph node metastasis rather than visceral metastasis. Patients with extensive metastatic tumor load or visceral crisis were not specifically excluded, but these patients are generally treated with combination immune checkpoint inhibitor treatment or (if BRAF V600E mutated) with MAPK inhibitors rather than anti-PD1 monotherapy. As a result from this, a possible bias towards a lower M-stage in our st. IV patients is possible.

Ethics oversight

UZ Leuven Medical Ethical Committee

Note that full information on the approval of the study protocol must also be provided in the manuscript.

Flow Cytometry

Plots

Confirm that:

- The axis labels state the marker and fluorochrome used (e.g. CD4-FITC).
- The axis scales are clearly visible. Include numbers along axes only for bottom left plot of group (a 'group' is an analysis of identical markers).
- All plots are contour plots with outliers or pseudocolor plots.
- A numerical value for number of cells or percentage (with statistics) is provided.

Methodology

Sample preparation

Tumor samples and metastatic organs were isolated from the corresponding mouse melanoma models (allograft or GEMMs) were rinsed in cold Dulbecco's Phospho-Buffered Saline (DPBS). Tissues were minced into small pieces and with sterile scalpels or scissors and incubated 30 minutes in a heater-shaker at 37°C 800 rpm in digestion buffer. Tissue samples from each mouse model were enzymatically digested using Liberase (300µg/ml, Sigma Aldrich, #5401127001) and DNaseI (1 mg/ml) diluted in serum free medium (DMEM) and incubate for 30 minutes at 37°C. For primary back skin tumors in the Tyr::CreERT2;BRafV600E/+;Ptenl/l model, digestion buffer consisted of 0.8 mg/mL DNase I (Sigma-Aldrich, Cat#11284932001) and 2 ng/mL collagenase P (Sigma-Aldrich, Cat#11249002001) diluted in serum free medium (DMEM). Digestion mix was inactivated with DMEM containing 10% FBS. To remove excess of red blood cells, samples when needed were incubated for 5 min in red blood lysis buffer (Thermo Fisher, Cat#A1049201) at room temperature according to the manufacturer's instructions. Single cells were separated from remaining tissue using 40 µm Falcon Cell Strainers (Corning) and resuspended either in FACs buffer (PBS supplied with 2% fetal bovine serum and 2 mM EDTA) or in 0.04% BSA. Then, cells were sorted using BD FACSAria™ Fusion Flow Cytometer. For in vitro experiments, cells were trypsinized, resuspended in FACS buffer (2% FBS, 1mM EDTA, 25 mM, HEPES pH7.0 in phosphate-buffered saline) and then filtered through a 40-µm strainer. Cells were analyzed by FACS (SONY MA9000 or BD Fortessa X-20).

Instrument

BD FACSAria fusion cell sorter was used for all the in vivo experiments performed and SONY MA9000 or BD Fortessa X-20 for the in vitro experiments to assess melanoma-EC circuitry.

Software

Facs diva 9.0.1 was used to collect and analyze cells from BD FACSAria fusion and BD Fortessa X-20. Sony MA900 cell sorter software was used to sort/analyze cells in SONY MA900.

Cell population abundance

Tdomato+ cells were isolated from two different melanoma mouse models as follows:
 - Prrx1::CreER-GFP;Tyr-NRASQ61K^o;Ink4a-/-;ROSA26RSLSL-tdTomato/LSL-tdTomato mice: In primary tumors tdomato+ cells constituted 8% and 2% of ACTA2 negative population in early and late labelled tumors, respectively. In lung metastasis, tdomato+ cells constituted 4,2% and 1,3% of ACTA2 negative population in early and late labelled tumors, respectively.
 - Tyr::CreERT2/+;BRafCA/+;Ptenl/l;ROSA26RSLSL-tdTomato/LSL-tdTomato: tdomato+ sorted cells constituted 13,5% of the singlets.
 Purity was assessed by performing scRNA seq experiments.

Gating strategy

For Prrx1::CreER-GFP;Tyr-NRASQ61K^o;Ink4a-/-;ROSA26RSLSL-tdTomato/LSL-tdTomato mice, tdomato+ cells first were gated

Gating strategy

based on FSC-DAPI (for living cells, DAPI negative), followed by exclusion of doublets based on FSC/SSC parameters (A, H and W). Next ACTA-2 positive cells were excluded based on a ACTA2-FSC plot and tdTomato positive cells were sorted. The ACTA2 gating was set based on an FMO control of the same sample and tdtomato on non-induced mice. For co-culture experiments, watermelon infected cells were gated based on FSC vs SSC. Debris were excluded based on the position on the FSC. Doublet exclusion was based on FSC-A versus FSC-H. DAPI staining was used to exclude dead cells using an unstained cells as negative control. mNeon positive cells were selected using non-infected cells as negative control. mCherry fluorescence was evaluated within mNeon-positive population, allowing to exclude Bend3 cells. Watermelon expressing cells non treated with doxycycline were used as a negative control. The compensation was performed using single staining. Matrix was calculated either automatically (Sony MA900 software) or manually using FlowJo.

Tick this box to confirm that a figure exemplifying the gating strategy is provided in the Supplementary Information.